Monthly Notices
of the
ROYAL ASTRONOMICAL SOCIETY

MNRAS **452,** 1841–1860 (2015) doi:10.1093/mnras/stv1407

Decreased specific star formation rates in AGN host galaxies⋆

T. Taro Shimizu,[1]† Richard F. Mushotzky,[1] Marcio Meléndez,[1] Michael Koss[2] and David J. Rosario[3]

[1]*Department of Astronomy, University of Maryland, College Park, MD 20742, USA*
[2]*Institute for Astronomy, Department of Physics, ETH Zurich, Wolfgang-Pauli-Strausse 27, CH-8093 Zurich, Switzerland*
[3]*Max-Planck-Institut für Extraterrestrische Physik (MPE), Postfach 1312, D-85741 Garching, Germany*

Accepted 2015 June 23. Received 2015 June 19; in original form 2015 January 22

ABSTRACT

We investigate the location of an ultra-hard X-ray selected sample of active galactic nuclei (AGN) from the *Swift* Burst Alert Telescope (BAT) catalogue with respect to the main sequence (MS) of star-forming galaxies using *Herschel*-based measurements of the star formation rate (SFR) and M_*'s from Sloan Digital Sky Survey photometry where the AGN contribution has been carefully removed. We construct the MS with galaxies from the *Herschel* Reference Survey and *Herschel* Stripe 82 Survey using the exact same methods to measure the SFR and M_* as the *Swift*/BAT AGN. We find that a large fraction of the *Swift*/BAT AGN lie below the MS indicating decreased specific SFR (sSFR) compared to non-AGN galaxies. The *Swift*/BAT AGN are then compared to a high-mass galaxy sample (CO Legacy Database for *GALEX* Arecibo SDSS Survey, COLD GASS), where we find a similarity between the AGN in COLD GASS and the *Swift*/BAT AGN. Both samples of AGN lie firmly between star-forming galaxies on the MS and quiescent galaxies far below the MS. However, we find no relationship between the X-ray luminosity and distance from the MS. While the morphological distribution of the BAT AGN is more similar to star-forming galaxies, the sSFR of each morphology is more similar to the COLD GASS AGN. The merger fraction in the BAT AGN is much higher than the COLD GASS AGN and star-forming galaxies and is related to distance from the MS. These results support a model in which bright AGN tend to be in high-mass star-forming galaxies in the process of quenching which eventually starves the supermassive black hole itself.

Key words: stars: formation – galaxies: active – galaxies: nuclei – galaxies: Seyfert – infrared: galaxies.

1 INTRODUCTION

The link between supermassive black holes (SMBH) and their host galaxies has been evident for many years through the study of correlations between large-scale host galaxy properties and SMBH mass. Tight correlations were found with bulge stellar velocity dispersion (Ferrarese & Merritt 2000; Gebhardt et al. 2000; Gültekin et al. 2009), bulge luminosity (e.g. Magorrian et al. 1998), and bulge mass (Kormendy & Richstone 1995; Marconi & Hunt 2003; Häring & Rix 2004) suggesting a coevolution of the SMBH with the host galaxy. The question that remains however is how two seemingly disjoined objects can influence each other over an extremely large range of physical scales. Using a simple estimate of the sphere of influence for an SMBH ($r_{\rm sph} = GM/\sigma^2$; Peebles 1972) and a typical SMBH mass of $10^8\,{\rm M}_\odot$ and stellar velocity dispersion, $\sigma = 200\,{\rm km\,s^{-1}}$, $r_{\rm sph} \sim 10$ pc whereas the size of the bulge is roughly several kpc (e.g. Simard et al. 2011). Therefore, any influence from the SMBH must be able to extend over three orders of magnitude in physical scale.

Active galactic nuclei (AGN), the phase where the SMBH is vigorously accreting material and growing, are thought to supply the necessary energy to influence the galaxy on large scales (e.g. Silk & Rees 1998). This leads to a feedback cycle wherein the galaxy supplies cold gas that ignites the AGN and fuels star formation, and the AGN then returns energy and/or momentum to the galaxy that shuts off both accretion and star formation. The explicit feedback mechanism that runs this cycle is currently not well understood but is thought to be either large-scale outflows (Kaviraj et al. 2011; Cimatti et al. 2013; Veilleux et al. 2013; Harrison et al. 2014) or radio jets (Best 2007; Dubois et al. 2013, for a review see Fabian 2012).

⋆*Herschel* is an ESA space observatory with science instruments provided by European-led Principal Investigator consortia and with important participation from NASA.

†E-mail: tshimizu@astro.umd.edu

Theoretical simulations have also shown that adding AGN feedback reproduces well the observed mass and luminosity functions while an absence produces too many blue, high-mass galaxies (e.g. Croton et al. 2006).

Early evidence for the quenching of star formation due to AGN came from studying the colours and stellar masses of large samples of both non-AGN and AGN host galaxies. Whereas the non-AGN sample clearly separates into two populations on a colour–magnitude or colour–mass diagram, one with red colours (i.e. red sequence thought to be quiescent galaxies) and one with blue (i.e. blue cloud thought to be strongly star-forming galaxies; Strateva et al. 2001), AGN host galaxies were found to be concentrated between them, displaying 'green' colours (e.g. Nandra et al. 2007; Silverman et al. 2008; Hickox et al. 2009). Initially, this was interpreted as AGN preferentially occurring in galaxies that have had their star formation recently quenched (Martin et al. 2007; Salim et al. 2007; Schawinski et al. 2009) and are in transition from the blue cloud to the red sequence. Optical colours, however, can be imprecise tracers of star formation, especially in the presence of strong intrinsic dust absorption (e.g. Cardamone et al. 2010) that obscures recent star formation and causes a reddening of the colours that is not due to a reduction of star formation. Green colours can also just be an indication of a mixture of old and new stellar populations and not necessarily a 'transition' between the two populations. Further, recent studies that mass-match non-AGN galaxy samples to AGN host galaxies reveal that the difference in optical colours virtually disappears (Silverman et al. 2009; Pierce et al. 2010; Rosario et al. 2013a, 2013b).

Far-infrared (FIR) emission ($\lambda > 40\,\mu$m) is essentially immune to reddening effects while also being a direct tracer of recent star formation. Dust in the galaxy is heated by UV photons from recently formed OB stars, which then re-emit in the mid-to-far-infrared regime (Draine 2003) creating a strong correlation between the FIR luminosity and star formation rate (SFR) of a galaxy (Kennicutt 1998; Kennicutt & Evans 2012). Furthermore, AGN are not thought to strongly affect the FIR (e.g. Netzer et al. 2007), and thus the FIR is more robust compared to other SFR indicators such as UV continuum and Hα line emission that are mainly used in non-AGN galaxy studies.

The *Herschel Space Observatory* (Pilbratt et al. 2010) opened a window into the FIR universe with the unprecedented sensitivity of both the Photodetector Array Camera and Spectrometer (PACS; Poglitsch et al. 2010) and Spectral and Photometric Imaging Receiver (SPIRE; Griffin et al. 2010) instrument extending the broad-band spectral energy distributions (SEDs) out to 500 μm and allowing an accurate estimate of the FIR luminosity of more objects than allowed by previous FIR telescopes (i.e. *Infrared Astronomical Satellite, IRAS*; Neugebauer et al. 1984). In this study, we utilize *Herschel* to measure the SFRs of a large and relatively unbiased sample of AGN and compare their location on the SFR–stellar mass (M_*) diagram with that of the general star-forming (SF) galaxy population, which forms a 'main sequence' (MS).

The MS is the observed tight correlation between the stellar mass and SFR of a normal SF galaxy and has been confirmed in depth by many studies (e.g. Brinchmann et al. 2004; Elbaz et al. 2007, 2011; Noeske et al. 2007; Rodighiero et al. 2010; Whitaker et al. 2012; Magnelli et al. 2014). This correlation seems to exist up to at least $z \sim 2$ (e.g. Elbaz et al. 2011; Whitaker et al. 2012) and possibly all the way to $z \sim 4$ (Bouwens et al. 2012; Heinis et al. 2014), with only the normalization changing as a function of redshift, shifting to higher SFRs at earlier epochs. This discovery has changed theories of galaxy evolution from one that is merger-driven to one that is driven more by internal secular processes. Elbaz et al. (2011) showed that galaxies that live above the MS are much more compact with a higher SFR surface density, indicative of a major merger. MS galaxies, though, have disc-like morphologies inconsistent with a recent merger (Wuyts et al. 2011) that suggests star formation is triggered by internal processes such as disc instabilities.

In the past, the question of where AGN fit into the picture was unclear because most MS studies purposely excluded AGN due to its messy contribution to SFR indicators. However, with *Herschel*, more accurate estimates of the SFRs for AGN host galaxies can be calculated as well as better detection rates. For example, both Mullaney et al. (2012b) and Rosario et al. (2013b), using deep observations of large fields, examined the SF properties of X-ray selected AGN. Both came to the conclusion that AGN primarily reside in MS galaxies, calling into question the long-held idea that AGN host galaxies are in the process of quenching star formation. If most AGN are in MS galaxies, this could indicate that moderate-luminosity AGN are simply coincidental with a large cold gas reservoir that also fuels star formation (Vito et al. 2014).

In this paper, we seek to fully investigate the location of AGN on the SFR–M_* plane using *Herschel* observations of *Swift*/BAT selected AGN. These are ultra-hard X-ray confirmed AGN at low redshift using a selection method that is unbiased with respect to both obscuration and host galaxy contamination. We calculate SFRs using *Herschel* photometry and a simple model to disentangle star formation and AGN contributions and combine them with estimates of the stellar mass using AGN-subtracted Sloan Digital Sky Survey (SDSS) photometry from Koss et al. (2011). The SFRs and M_*'s are then compared to a local normal SF galaxy sample to define the MS as well as a sample of galaxies purely selected on stellar mass. Finally, we discuss the implications of our results and compare them to previous studies. Throughout this paper, we use a Λ cold dark matter cosmology with $H_0 = 70\,\mathrm{km\,s^{-1}\,Mpc^2}$, $\Omega_\mathrm{m} = 0.3$, and $\Omega_\Lambda = 0.7$. Luminosity distances were calculated using this cosmology along with redshifts taken mainly from the NASA/IPAC Extragalactic Database (NED),[1] except for those objects with $z < 0.01$ where we used measured distances from the Extragalactic Distance Database.[2] We either use or correct for a Chabrier or Kroupa initial mass function (IMF) for all SFR calculations.

2 SAMPLES AND OBSERVATIONS

2.1 *Swift*/BAT AGN

Our parent sample of AGN was drawn from the 58-month *Swift* Burst Alert Telescope (BAT) (Gehrels et al. 2004; Barthelmy et al. 2005) catalogue (Baumgartner et al. 2013) with a redshift cutoff of $z < 0.05$, totalling 313 AGN (149 Seyfert 1-1.5s, 157 Seyfert 1.8-2s, 6 LINERs, and 1 unidentified AGN). The catalogue is the result of continuous monitoring by *Swift*/BAT of the entire sky in the 14–195 keV energy range. These high energies allow for an unambiguous detection of AGN with little to no contamination from the host galaxy and significantly reduced selection effects due to obscuration.

All 313 AGN were observed by the *Herschel Space Observatory* with 291 part of our programme (PI: R. Mushotzky, PID: OT1_rmushotz_1) and the remaining 22 obtained from other programmes publicly available on the *Herschel* Science Archive. The

[1] http://ned.ipac.caltech.edu/
[2] http://edd.ifa.hawaii.edu/

sample was imaged by both the PACS and SPIRE instruments providing, for the first time, sensitive FIR photometry from 70 to 500 μm for a large, ultra-hard X-ray selected sample of AGN. Detailed descriptions of the reduction and analysis of the PACS and SPIRE images are given in Meléndez et al. (2014) and Shimizu et al. (in preparation), but we provide a brief summary here.

PACS and SPIRE together imaged the sample in five broad-bands: 70 and 160 μm (PACS) and 250, 350, and 500 μm (SPIRE). Level 0 (raw) data were reduced to Level 1 using the standard pipeline provided by the *Herschel* Interactive Processing Environment (Ott 2010) v8.0. Maps were produced from the Level 1 data using SCANAMORPHOS (Roussel 2013) v19.0, a software package that takes advantage of the redundancy inherent in the scanning procedure of *Herschel* to remove both thermal and non-thermal low-frequency noise. Circular and elliptical apertures with radii chosen visually to encompass the entirety of the FIR emission were then used to extract the photometry for each waveband. 1σ errors for the photometry were determined using a combination of the pixel-by-pixel errors in the aperture, an estimate of the root mean square of the background, and calibration uncertainty.

In addition to *Herschel* observations, Koss et al. (2011) analysed optical images of 185 BAT AGN from the SDSS and Kitt Peak National Observatory. Using GALFIT (Peng et al. 2002), they were able to accurately measure the host galaxy light by subtracting out the central point source due to the AGN. Reliable stellar masses for the BAT AGN host galaxies were then estimated using standard stellar population models. Because the Koss et al. (2011) BAT sample was chosen from the 22-month catalogue (Tueller et al. 2010), 45/185 were not observed with *Herschel*, reducing the sample to 140 AGN. Furthermore, Koss et al. (2011) flagged 18/140 objects for incomplete point spread function (PSF) subtraction from the *griz* images, so we choose not to include these sources resulting in a final sample of 122 AGN, including 46 Sy 1s, 72 Sy 2s, and 4 LINERs, where we define a Sy 1 as Sy 1-1.5 and Sy 2 as Sy 1.8-2. The reason for the discrepancy between the number of Sy 1s and Sy 2s is that all 18 of the objects that were flagged for incomplete PSF subtraction are Sy 1s.

2.2 *Herschel* Reference Survey

To form the MS, we need a large and complete sample of SF galaxies that do not host an AGN but have been observed at the same wavelengths allowing for a consistent determination of both the SFR and stellar mass. For these reasons, we chose the *Herschel* Reference Survey (HRS; Boselli et al. 2010), a guaranteed time *Herschel* key project that imaged 323 *K*-band selected galaxies from 100 to 500 μm. The HRS spans all morphological types and was volume limited to contain galaxies between 15 and 25 Mpc away. Even though our sample stretches out to $z = 0.05$ (∼200 Mpc), the HRS represents the best sample of local SF galaxies to compare with given that both have been observed by *Herschel* as well as other telescopes including the *Wide-field Infrared Survey Explorer* (*WISE*; Wright et al. 2010), the *Galaxy Evolution Explorer* (*GALEX*; Martin et al. 2005), and SDSS.

The HRS PACS and SPIRE images were analysed in Cortese et al. (2014) and Ciesla et al. (2012) producing photometry at 100, 160, 250, 350, and 500 μm. We applied the same corrections to the SPIRE photometry as described in Cortese et al. (2014) due to changes in the SPIRE calibration and beam size. The corrections reduce the SPIRE flux densities by 7, 6, and 9 per cent at 250, 350, and 500 μm, respectively.

A subset of the HRS are galaxies within the Virgo Cluster and have been affected by the dense environment through the stripping of their gas (Boselli et al. 2006). The dust content of these galaxies has also been shown to be affected by the environment (Cortese et al. 2010, 2012a). Therefore, following Ciesla et al. (2014), we restrict the HRS sample to only those galaxies that are not 'H I-deficient' as defined in Boselli et al. (2012) which reduces the sample to 146 galaxies.

2.3 COLD GASS

While the HRS represents a sample that was observed using the same telescopes, it is limited in its range of stellar mass especially above 10^{10} $M_\odot$. For a complete comparison to the BAT AGN, we supplemented HRS with the CO Legacy Database for GASS (COLD GASS; Saintonge et al. 2011a), a 366 galaxy subsample of the *GALEX* Arecibo SDSS Survey (GASS; Catinella et al. 2010). The GASS sample consists of ∼1000 galaxies randomly selected such that every galaxy lies within the footprint of the SDSS spectroscopic survey, the Arecibo Legacy Fast Arecibo L-band Feed Array survey, and the *GALEX* Medium Imaging Survey. The galaxies were also selected to have a redshift range $0.025 < z < 0.05$ and a stellar mass between 10^{10} and $10^{11.5}$, both of which match very well to the BAT AGN. 366 galaxies were randomly selected from GASS to form the COLD GASS sample and have deep CO(1–0) imaging with the IRAM 30-meter telescope. COLD GASS then represents a completely unbiased sample of galaxies above 10^{10} $M_\odot$.

As described in Catinella et al. (2010) and Saintonge et al. (2011a), both GASS and COLD GASS were selected to have a uniform $\log M_*$ distribution. The stellar mass distribution that is observed, however, is more heavily weighted towards lower mass galaxies (see fig. 1 of Saintonge et al. 2011a). Therefore, Saintonge et al. (2011a) constructed 50 representative subsamples of COLD GASS that match the observed M_* distribution. Each subsample contains between 200 and 260 galaxies and can be used to test the robustness of any relation that might be observed. Throughout this paper, we explicitly note whether the full COLD GASS sample, an average of the representative subsamples, or a single representative subsample is being used.

Because COLD GASS was selected in an unbiased way, the sample contains a mixture of galaxy types from SF to quiescent to AGN. To determine the type of each galaxy in COLD GASS, we cross-matched the sample with the MPA-JHU SDSS DR7 spectroscopic catalogue.[3] In this catalogue, galaxies that have SDSS optical spectra were classified according to their location on the standard BPT diagram (Baldwin, Phillips & Terlevich 1981). Brinchmann et al. (2004) describe the details of the classification.[4] Galaxies were separated into six groups: SF, low-S/N SF, AGN, composite, LINER, and quiescent. For the purposes of comparison with the BAT AGN, we combined the SF and low-S/N SF groups into a single SF group and the AGN and composite groups into a single AGN+composite group. We combine the AGN and composite group because after cross-matching the BAT AGN with the same SDSS DR7 sample, we find that almost all are classified as an AGN or composite galaxy.

[3] http://www.mpa-garching.mpg.de/SDSS/DR7/ and http://home.strw.leidenuniv.nl/jarle/SDSS/

[4] We note that Saintonge et al. (2012) used a more conservative method to classify AGN in the COLD GASS. A galaxy was considered an AGN if $\log$ [N II/Hα] > -0.22 and $\log$ [O III/Hβ] > 0.48. This led to a much lower fraction of AGN in their analysis (6 per cent) compared to this work (30 per cent).

The COLD GASS AGN+composite subsample then represents an ideal optically selected sample of AGN to compare with the BAT AGN, while the SF and quiescent sample represent ideal non-AGN samples. We denote the different subsamples in the following way: SF as CGS, AGN+composite as CGA, LINERs as CGL, and quiescent as CGQ.

2.4 *Herschel* Stripe 82 Survey

With the HRS and COLD GASS samples we have one that matches the photometry available to the BAT AGN (HRS) and one that more closely matches the physical properties of the BAT AGN host galaxies (COLD GASS). HRS lacks galaxies at the high stellar mass of the BAT AGN whereas COLD GASS lacks *Herschel* and *WISE* photometry to allow for a consistent comparison between SFRs. Therefore, we use a third comparison sample to the BAT AGN, the *Herschel* Stripe 82 Survey (HerS; Viero et al. 2014), that bridges the gap between HRS and COLD GASS.

HerS is a 79 deg^2 survey of SDSS Stripe 82 with *Herschel*/SPIRE at 250, 350, and 500 μm. Viero et al. (2014) produced the catalogue of HerS sources while Rosario et al. (in preparation) calculated SFRs based on FIR luminosities. Given its small area, the volume covered at low redshift is smaller than that of both the COLD GASS and BAT samples which means HerS is rather incomplete at high stellar masses ($>10.5\,M_\odot$). However, it is still better than the HRS and has *Herschel* photometry available, albeit only from the SPIRE instrument.

We selected our HerS sample from Rosario et al. (in preparation), who matched HerS sources from Viero et al. (2014) with the SDSS MPA-JHU DR7 catalogue. Because the HerS catalogue assumes that all galaxies are point sources, Rosario et al. (in preparation) limited their sample to $z > 0.02$. We further limit the sample to $z < 0.08$ to match the BAT AGN while also pushing out to a slightly larger volume to populate the high-mass end better without significantly affecting our results. After cutting sources which do not have a measured stellar mass as well as sources with low-S/N (<3) emission lines (only five objects), this results in a final HerS sample of 517 objects. Due to the combined magnitude cut from the SDSS and the limited sensitivity of SPIRE from which the HerS catalogue was built, Malmquist bias can be a problem. However, because of the relatively low redshift nature of our sample, we do not expect it to largely bias our results.

The HerS sample was also split into some of the same classifications as COLD GASS using the BPT diagram. HerS contains both an SF and AGN population and will be designated as HerS SF and HerS AGN. The HerS AGN, just as CGA, is a combination of the AGN and composite classifications. Within HerS, there is also an uncertain classification which indicates a galaxy that is missing or has upper limits for at least one of the four key lines needed to classify it using the BPT diagram.

3 SFR ESTIMATION

The unique *Herschel* data provide a means for determining accurate SFRs. IR emission has long been used as a calibrator for star formation (see Kennicutt 1998, for a review), because it probes the dust population that reprocesses the UV emission from young stars (e.g. Draine 2003). The specific wavelength range of *Herschel* covers the bulk of the IR emission from dust including the characteristic FIR bump typically seen in SF galaxies (e.g. Dale et al. 2007) allowing for precise measures of the total IR luminosity and thus the SFR, especially for AGN host galaxies where many of the often used SFR indicators (e.g. Hα, UV continuum) can be substantially contaminated by AGN-related emission.

Many SED-fitting packages exist in the literature ranging from template-based models to full dust radiative transfer models. However, given the low number of data points for our SEDs (at most seven), we chose to fit our SEDs with the model described in Casey (2012), which is a combination of an exponentially cutoff mid-infrared (MIR) power law and a single-temperature greybody. Details and results of the SED fitting for the BAT AGN will be given in a forthcoming paper (Shimizu et al., in preparation); however, we provide example fits to both the BAT AGN and HRS in Appendix A as well as a brief overview of the fitting procedure. In Section 6.1, we discuss extensively and test whether this model introduces systematic biases especially related to the decomposition of the SED.

The *Herschel* photometry constrains the greybody component, but we need additional shorter wavelength data to constrain the power-law component. Therefore, we cross-correlated our sample with the *WISE* (Wright et al. 2010) All-Sky Release Catalog on the IRSA website.[5] We only use the 12 ($W3$) and 22 μm ($W4$) photometry to avoid contamination by the stellar population in the host galaxy. *WISE* photometry for the HRS was taken from Ciesla et al. (2014).

For consistency, we fit both the BAT AGN and HRS galaxies using the Casey (2012) model even though the HRS galaxies do not host an AGN or are classified as ultra-luminous infrared galaxies (ULIRGs). In this way, we can account for a portion of MIR emission that is due to normal star formation rather than AGN heated dust. We fit all BAT AGN and HRS galaxies with at least four detected photometric points. This restriction ensures quality photometry for each galaxy and removes only a further 9 and 11 galaxies from the BAT AGN and HRS sample, respectively, for final sample sizes of 113 and 135. We determine three luminosities for each galaxy: a total IR luminosity ($L_{\rm TIR}$), an MIR power-law luminosity ($L_{\rm MIR}$), and a greybody luminosity ($L_{\rm Grey}$). Each one was calculated by integrating the best-fitting model from 8 to 1000 μm. $L_{\rm TIR}$ is the luminosity from integrating over the total model while $L_{\rm MIR}$ is from only integrating the MIR power-law component, and $L_{\rm Grey}$ is from the greybody component.

Star formation rates are then calculated using one of these IR luminosities and the equation from Murphy et al. (2011),

$$\mathrm{SFR_{IR}} = \frac{L_{\rm IR}\ [\mathrm{erg\ s^{-1}}]}{2.57 \times 10^{43}}. \quad (1)$$

For the HRS galaxies, $L_{\rm IR} = L_{\rm TIR}$ since there is no AGN to contribute to the IR emission. For the BAT AGN, however, we use $L_{\rm IR} = 4/3 L_{\rm Grey}$. The 4/3 is a correction factor to account for MIR emission from star formation. To determine it, we calculated the average ratio of $L_{\rm MIR}/L_{\rm Grey}$ for the HRS sample, which contain no AGN, and found it to be narrowly distributed around 1/3. This means that only using $L_{\rm Grey}$ to determine the SFR underestimates it by 1/3 so we need to multiply $L_{\rm Grey}$ by 4/3 as a correction.

While FIR emission probes dust-obscured star formation, the UV continuum is a measure of unobscured star formation by tracing the direct light from young massive stars. Hence, a complete census of star formation can be found by combining measurements from both wavebands. AGN are strong emitters in the UV though, so only Seyfert 2 galaxies will have reliable UV photometry to combine with the FIR for an SFR. Using *GALEX* far-UV (FUV)

[5] http://irsa.ipac.caltech.edu/Missions/wise.html

data from the GCAT catalogue (Bianchi, Conti & Shiao 2014) for the BAT AGN Seyfert 2s and the same from Boselli et al. (2013) for the HRS, we calculated dust-corrected UV SFRs. We found that using UV SFRs for both the HRS and BAT AGN Seyfert 2s had no effect on the results of this paper. Thus, we choose to use the FIR only SFRs to allow a larger BAT AGN sample (Seyfert 1s and 2s).

The COLD GASS sample unfortunately was not observed with *Herschel* and does not allow for the same calculation of the SFR. We use the SFRs provided in Saintonge et al. (2011b) which were calculated by fitting SDSS and *GALEX* photometry to Bruzual & Charlot (2003) models. Saintonge et al. (2011b) compared these SFRs to those inferred from combined *GALEX* FUV and *Spitzer* 70 μm data finding a strong correlation with only a scatter of 0.22 dex and indicating that FIR-based SFRs are consistent with optical–UV ones. We recognize that the Saintonge et al. (2011b) comparison however did not use any *Herschel* photometry, but three calibration analyses[6] show that *Spitzer* and *Herschel* produce consistent fluxes. Further, Domínguez Sánchez et al. (2014) recently showed that SFRs calculated from FIR SED fitting are consistent (with large scatter especially for pure AGN and quiescent galaxies) with the SFRs inferred from the MPA-JHU SDSS spectral analysis. Based on all these indirect tests, we are confident that the COLD GASS SFRs are consistent with the *Herschel*-based ones we use for the HRS and BAT AGN in a way that does not affect the results of this paper.

For the HerS sample, the SFRs were estimated by fitting the SPIRE 250 μm and *WISE* 22 μm fluxes to the Dale & Helou (2002, hereafter DH02) templates. Each of the 64 templates represents a different value of α, where α is the power-law index for the distribution of dust mass over heating intensity in a galaxy. χ^2-minimization was used to scale each of the 64 templates to the observed fluxes in the HerS sample, and then the template with the lowest χ^2 was chosen as the best fit. The best-fitting template was integrated between 8 and 1000 μm to calculate $L_{\rm IR}$ and converted to an SFR using the SFR–$L_{\rm IR}$ relation from Kennicutt (1998) adjusted for a Chabrier IMF (lowered by a factor of 1.7). In the absence of *WISE* 22 μm photometry, α was fixed at -2.0.

This is a slightly different method from the one used for the HRS and BAT AGN. To test for systematics, we fit the HRS galaxies with 250 and 22 μm detections using the DH02 method and compared the SFRs. A linear fit to the two SFRs reveals a slope of 1.0 and an offset of 0.11 dex with the SFRs determined from the Casey (2012) and equation (1) higher than the ones from DH02 and the relation from Kennicutt (1998). Therefore, we adjust all of the HerS SFRs by adding a constant of 0.11 dex.

4 STELLAR MASS ESTIMATES

SFRs are only one-half of the MS; stellar masses are also needed for the galaxies. Cortese et al. (2012b) calculated the stellar masses of the HRS using the relation from Zibetti, Charlot & Rix (2009):

$$\log(M_*/L_i) = -0.963 + 1.032(g-i), \quad (2)$$

where M_* is the stellar mass and L_i is the i-band luminosity, both in solar units. To be consistent, we also used this equation for the BAT AGN. The $g-i$ colour was calculated using the PSF-subtracted photometry from Koss et al. (2011). The stellar masses determined here correlate very well with the stellar masses from Koss et al. (2011) with a Pearson correlation coefficient, $r_{\rm P} = 0.85$ indicating a highly linear relationship. However, the Koss et al. (2011) values are systematically larger by a factor of $\sim$2.[7] Since the goal of this paper is to compare AGN with normal SF galaxies and not absolute measures of stellar mass and SFR, we choose to use equation (2) for the BAT AGN stellar masses. We performed the same calculation for the COLD GASS galaxies and compared these M_* with those provided in Saintonge et al. (2011b). We find the same strong correlation and the same systematic offset as the BAT AGN stellar masses so we choose to also use the stellar masses calculated in this paper for COLD GASS as well. The HerS stellar masses are taken from the MPA-JHU data base which used the same method as both Koss et al. (2011) and Saintonge et al. (2011b). However, we do not have g or i photometry for HerS so we apply a factor of 2 correction to them to match the stellar mass scale from equation (2).

5 RESULTS

5.1 Location of AGN in the SFR–M_* plane

One key issue in this analysis is which MS to use. Many authors have published MS relations (for a nice compilation, see Speagle et al. 2014); however, each relation was determined differently using different stellar mass estimates, SFR indicators, and redshift ranges. This has resulted in a large spread of values for both the slope and normalization of the MS, especially in the local universe. Therefore, we choose to calculate our own MS relation using only the HRS galaxies and the HerS SF galaxies since both the stellar masses and SFRs were calculated with comparable methods as for the BAT AGN. We use a linear bisector (Isobe et al. 1990) to fit the HRS+HerS data, resulting in the following equation:

$$\log({\rm SFR_{IR}}) = 1.01\log(M_*) - 9.87. \quad (3)$$

The scatter of the relation is 0.36 dex, similar to the scatter seen in other studies (e.g. Noeske et al. 2007; Peng et al. 2010). The slope and the normalization are slightly steeper and smaller, respectively, than that found in Peng et al. (2010), who analysed the SFRs and stellar masses of the entire local ($0.02 < z < 0.085$) SDSS population. The slope is much steeper than the $z = 0$ slope predicted using the Speagle et al. (2014) relation (0.5). This is possibly due to the addition of lower mass objects from HRS as well as differences in the measurement of the SFR and M_*. Further, due to the large scatter in MS relations measured at low redshift, Speagle et al. (2014) specifically did not include low-redshift studies in formulating their redshift-dependent MS relation. This is the reason we set out to formulate our own MS relation that uses a well-defined SF galaxy sample and measures of the SFR and stellar mass that are consistent between the non-AGN and AGN host galaxy samples.

[6] http://herschel.esac.esa.int/twiki/pub/Public/PacsCalibrationWeb/ExtSrcPhotom.pdf; http://herschel.esac.esa.int/twiki/bin/viewfile/Public/PacsCalibrationWeb?rev=1;filename=PICC-NHSC-TN-029.pdf; https://nhscsci.ipac.caltech.edu/pacs/docs/Photometer/PICC-NHSC-TR-034.pdf

[7] This is most likely due to the different stellar population models used in Zibetti et al. 2009. They used the 2007 version of the Bruzual & Charlot (2003) models that included a new prescription for thermally pulsing asymptotic giant branch stars. This decreases the stellar mass by a factor of 2 especially for SF galaxies. This has no effect on our results as long as all samples are on the same stellar mass scale.

Fig. 1 plots the HRS, BAT AGN, a randomly chosen representative subsample of COLD GASS, and the HerS sample on the SFR–M_* plane along with equation (3) and its scatter. Visually it is clear that a large fraction of the BAT AGN and COLD GASS lie either inside or below the MS. Table 1 quantifies the exact fraction of galaxies in five different regions. The different regions are divided according to $\Delta \log \mathrm{SFR} = \log \mathrm{SFR_{obs}} - \log \mathrm{SFR_{MS}}$, where $\mathrm{SFR_{obs}}$ is $\mathrm{SFR_{IR}}$ and $\mathrm{SFR_{MS}}$ is the SFR expected given the M_* of the galaxy using equation (3). $\Delta \log \mathrm{SFR}$ represents the distance a source is from the MS and given the nearly linear MS relation is proportional to specific SFR ($\mathrm{sSFR} = \mathrm{SFR}/M_*$). The five regions are defined as: above the MS ($\Delta \log \mathrm{SFR} > 1\sigma$), inside the MS ($1\sigma > \Delta \log \mathrm{SFR} > -1\sigma$), 1σ–2σ below the MS ($-1\sigma > \Delta \log \mathrm{SFR} > -2\sigma$), 2σ–3σ below the MS ($-2\sigma > \Delta \log \mathrm{SFR} > -3\sigma$), and 3σ below the MS ($\Delta \log \mathrm{SFR} < -3\sigma$) with σ equal to the observed scatter in the MS relationships (i.e. 0.36 dex). We break the 'below' region into three separate regions to judge how the sample is clustered. If all of the sources below the MS are in the 1σ region, then it could be argued that most of the AGN are MS galaxies and simply display a larger scatter. The fractions for the different COLD GASS subsamples are the average fraction over all 50 representative subsamples.

The numbers confirm the visual impression seen in Fig. 1 that the BAT AGN mainly live inside the MS or below it. 28 per cent lie inside the MS and 66 per cent lie below it from adding together the three 'below' regions. Only 5 per cent of the sample is above the MS. The sources below the MS are also well spread out between the 1σ, 2σ, and 3σ regions, showing the BAT AGN do not cluster near the edge of the MS and in fact a significant percentage (20 per cent) display SFRs more than 3σ below what is expected given their stellar masses.

For the COLD GASS sample as a whole, there seems to be a bimodal distribution with 33 per cent of galaxies inside the MS and 39 per cent $>3\sigma$ below it. This mirrors what has been extensively seen using optical colours and is another representation of the split into the blue cloud and red sequence. The BAT AGN do not display the same bimodality and overall have a very different distribution of $\Delta \log \mathrm{SFR}$ as shown in Fig. 2.[8] We ran Kolmogorov-Smirnov (K-S) tests to compare the BAT AGN with each COLD GASS representative subsample (see Section 2.3 for a description of the subsamples) and found that 0/50 tests returned a probability >5 per cent verifying that the two samples are not drawn from the same parent distribution.

The HerS sample differs from the COLD GASS and BAT AGN samples and is sharply peaked around $\Delta \log \mathrm{SFR} = 0$, signifying that most of the galaxies are on the MS. Indeed, 67 per cent of the total HerS sample lie inside the MS, while only 12 per cent are above and 21 per cent below. HerS likely does not reach as far below the MS as COLD GASS given that the parent sample was selected based on a SPIRE 250 μm detection. Using the Viero et al. (2014) 5σ depth for SPIRE 250 μm of 65 mJy and assuming a greybody with $T_{\mathrm{dust}} = 25$ K and $\beta = 2.0$, the minimum SFR detectable is 0.5 $\mathrm{M_\odot\ yr^{-1}}$, much higher than the level reached by COLD GASS and the BAT AGN. Even so, we again ran a K-S test between the

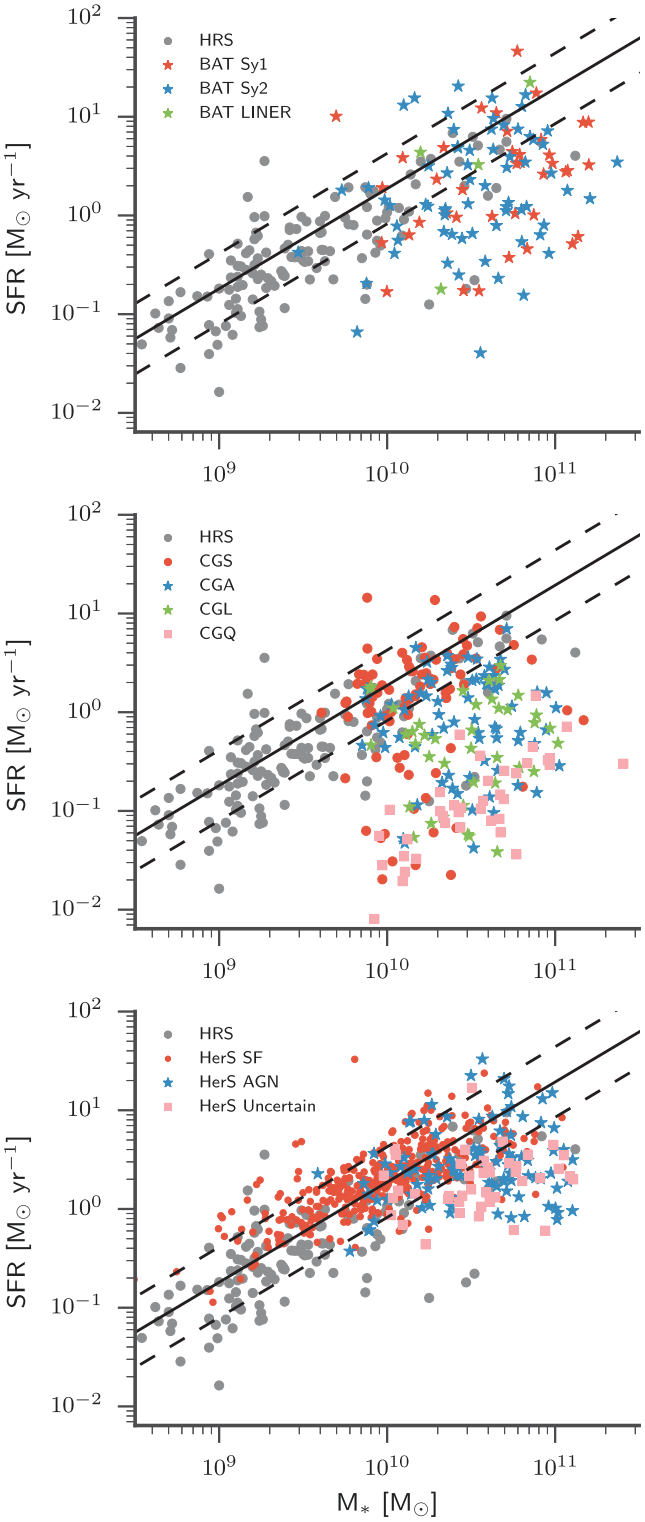

Figure 1. The relationship between SFR and M_* for the HRS (black dots), BAT AGN (top: coloured stars), a representative subsample of COLD GASS (middle: coloured symbols), and the HerS sample (bottom: coloured symbols). The solid line represents the MS relationship calculated using the IR-based HRS+HerS SFRs (equation 3). The dashed lines are the measured 1σ (0.32 dex) scatter in the relationship. A colour version of this figure is available online.

[8] We take this opportunity to explain that we choose to represent distributions of values using a kernel density estimate (KDE) rather than a histogram. This is due to the visualization of a histogram being highly dependent on the bin size, number of bins chosen, and the edges of the bins. A KDE represents each point in a data set with a specific kernel and sums all of them together. In this paper, we use a Gaussian kernel. The only tunable parameter is the kernel width for which we use 'Scott's rule' (Scott 1992), width $= N^{-1/5}$, where N is the number of data points.

Table 1. MS locations for BAT AGN and COLD GASS.

Sample (1)	Total (2)	Above MS (3)	Inside MS (4)	1σ–2σ below (5)	2σ–3σ below (6)	$>3\sigma$ below (7)
BAT AGN						
All	–	0.05	0.28	0.28	0.18	0.20
Sy 1	0.35	0.05	0.20	0.35	0.20	0.20
Sy 2	0.61	0.06	0.30	0.26	0.17	0.20
LINER	0.04	0.00	0.75	0.00	0.00	0.25
COLD GASS (CG)						
All	–	0.02	0.33	0.15	0.12	0.39
Star-forming (CGS)	0.37	0.04	0.62	0.12	0.05	0.16
AGN+comps (CGA)	0.30	0.02	0.28	0.23	0.15	0.34
LINER (CGL)	0.17	0.00	0.07	0.18	0.25	0.50
Quiescent	0.15	0.00	0.00	0.00	0.03	0.97
Herschel Stripe 82 (HerS)						
All	–	0.12	0.67	0.14	0.05	0.02
Star-forming	0.72	0.14	0.78	0.07	0.01	0.00
AGN+comps	0.19	0.08	0.48	0.25	0.10	0.09
Uncertain	0.08	0.02	0.21	0.42	0.28	0.07

Notes. (1) Sample and subsample names for the BAT AGN and COLD GASS. (2) Fraction of the total sample (i.e. BAT AGN and COLD GASS) that each subsample occupies. (3) Fraction of sample that is above the MS ($\Delta \log \mathrm{SFR} > 1\sigma$; $\sigma = 0.32$ dex). (4) Fraction of sample that is inside the MS ($1\sigma > \Delta \log \mathrm{SFR} > -1\sigma$). (5) Fraction of sample that is between 1σ and 2σ below the MS ($-1\sigma > \Delta \log \mathrm{SFR} > -2\sigma$). (6) Fraction of sample that is between 2σ and 3σ below the MS ($-2\sigma > \Delta \log \mathrm{SFR} > -3\sigma$). (7) Fraction of sample that is greater than 3σ below the MS ($\Delta \log \mathrm{SFR} < -3\sigma$). The COLD GASS fractions represent the average fractions over all 50 representative subsamples. Due to round-off errors, the sums across each row are not exactly equal to 1.

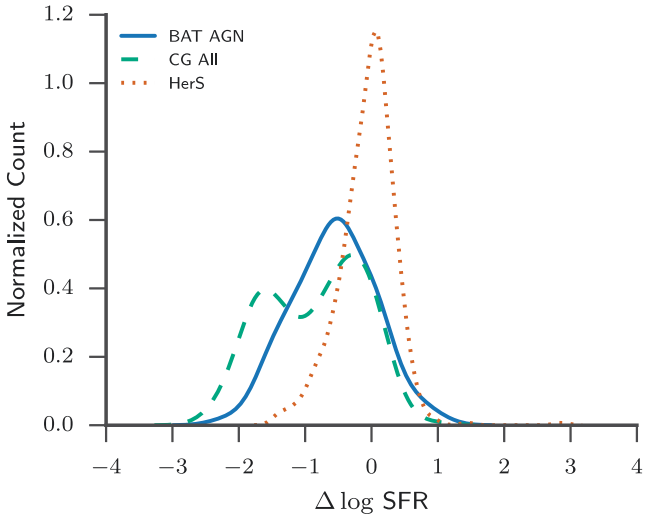

Figure 2. Kernel density estimate (KDE) of the logarithmic distance (Δ log SFR) from the MS for the BAT AGN, a representative subsample of COLD GASS, and the HerS sample. A colour version of this figure is available online.

BAT AGN and HerS and found $P_{\mathrm{K\text{-}S}} \ll 0.01$ indicating that they are drawn from different populations.

It is only when we separate the COLD GASS and HerS sample into their different classifications do we find a similarity. Fig. 3 shows the KDEs of $\Delta \log \mathrm{SFR}$ for the BAT AGN and each COLD GASS and HerS classification. The COLD GASS KDEs were calculated from a randomly chosen representative subsample. The BAT AGN are most similar to the CGA (e.g. the AGN population of COLD GASS), displaying lower values of $\Delta \log \mathrm{SFR}$ than CGS/HerS SF and higher values than CGL and especially CGQ. In fact, the percentages in each region for the BAT AGN and CGA are nearly identical except in the $>3\sigma$ region where there is a larger fraction of CGA. We again ran K-S tests for each of the 50 representative subsamples for COLD GASS and found that 48/50 CGA subsamples returned a probability >5 per cent indicating that the BAT AGN and CGA are consistent with the same parent population. 0/50 of the CGS, CGL, and CGQ subsamples returned a probability >5 per cent of being consistent with the BAT AGN. The K-S test between the BAT AGN and HerS AGN returned $P_{\mathrm{K\text{-}S}} = 0.002$ while the ones with HerS SF and HerS uncertain returned $P_{\mathrm{K\text{-}S}} \ll 0.001$ and $P_{\mathrm{K\text{-}S}} = 0.07$. Using the standard 5 per cent cutoff to determine if the samples originate from the same population would indicate that the BAT AGN are most similar to the HerS uncertain galaxy population. However, as we discuss above, this is most likely due to the lower SFR depth reached in HerS. Also the HerS uncertain classification is a more conservative classification and includes many galaxies that would have been classified using the Brinchmann et al. (2004) system including AGN and LINERs. The HerS AGN still show lower SFRs than the HerS SF sample with 48 per cent inside the MS compared to 78 per cent and 44 per cent below it compared to 8 per cent. Therefore, both an optically selected sample of AGN and an ultra-hard X-ray selected sample of AGN display the same property: they lie in between a strongly star-forming and quiescent group and suggests that AGN host galaxies are in transition between the two populations.

We note that while the K-S tests confirm that the BAT AGN and CGA are from the same population, both Table 1 and Fig. 3 show that the BAT AGN contain slightly more galaxies with higher SFRs while CGA contain slightly more quiescent galaxies. We hypothesize that this is due to the selection method for the two groups. The BAT AGN are X-ray selected by a method that is completely independent from the SF properties of the host galaxy while the CGA are selected by optical emission line ratios whose origin can be a mixture of AGN and star formation. If a galaxy is highly star-forming, optical emission line ratios are more likely to

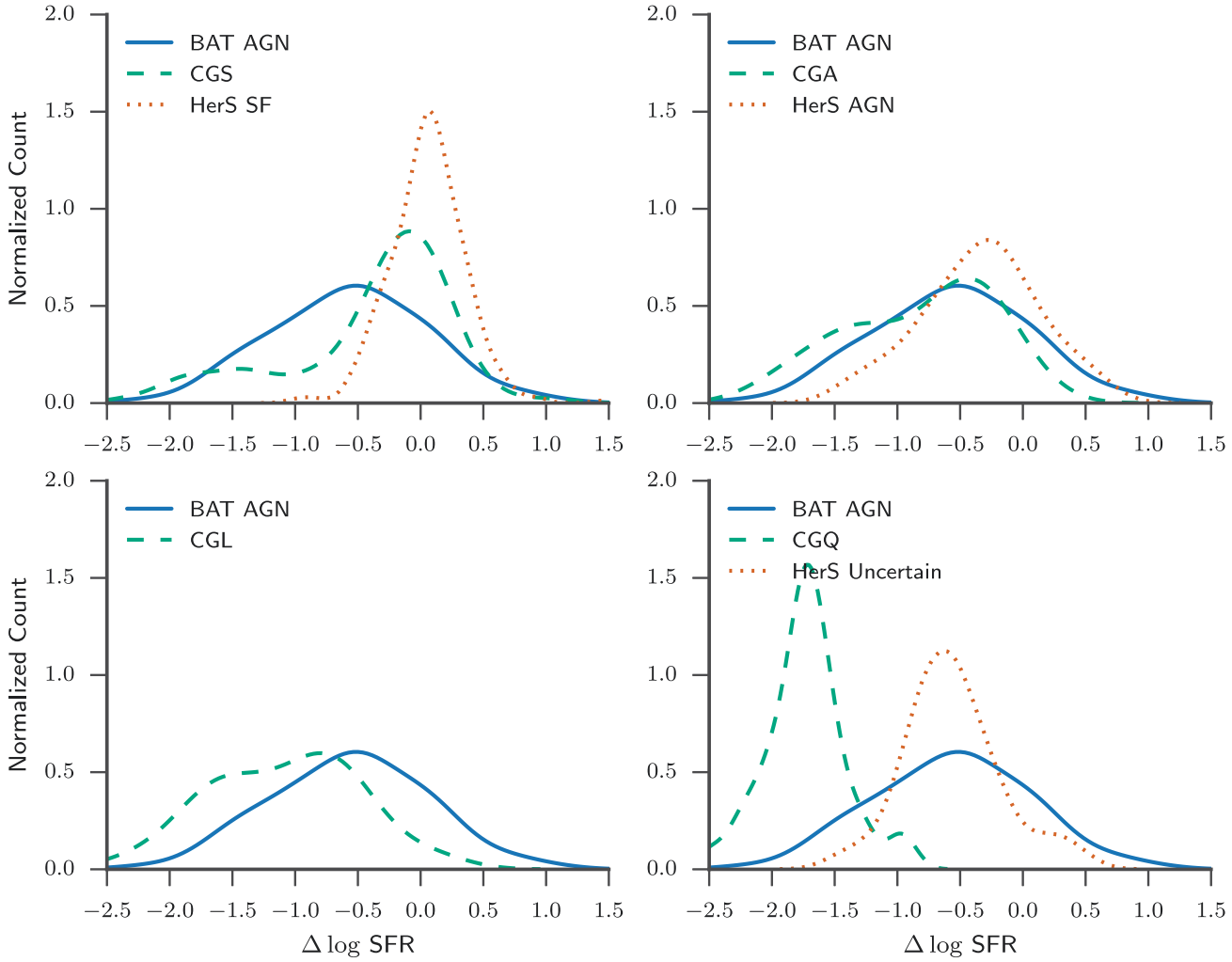

Figure 3. Same as Fig. 2 but with the COLD GASS subsample split into four classifications based on their location in the BPT diagram. CGS: SF galaxies. CGA: AGN and composite galaxies. CGL: LINERs. CGQ: quiescent galaxies. The HerS sample was split into three classifications (SF, AGN and composite, and uncertain). The BAT AGN galaxies show a similar distribution in Δ log SFR as the CGA and HerS AGN sample (upper right). A colour version of this figure is available online.

classify it as an SF galaxy rather than AGN or even composite [see Trump et al. (2015) for biases associated with line ratio selection of AGN]. Indeed, many of the BAT AGN above the MS are either involved in a merger or are known as starburst galaxies (e.g. Mrk 18, NGC 3079, NGC 7679).

Because the BAT survey is flux limited, it is biased against weak AGN, while COLD GASS, due to its selection from SDSS, can reach to lower AGN luminosities. If low-luminosity AGN are more associated with quiescent, early-type galaxies (e.g. Kauffmann et al. 2003), this would explain the larger fraction of the CGA group in the $>3\sigma$ region compared to the BAT AGN. In Section 5.4, we show that the CGA contain a larger fraction of elliptical galaxies than the BAT sample which have lower values of sSFR.

We also note that the BAT AGN and CGS have essentially the same fraction of galaxies in the $>3\sigma$ below region (16 per cent versus 14 per cent). This is seen in Fig. 3 as the long tail towards low Δ log SFR for CGS. However, this does not change the general result that the BAT AGN in general show lower levels of sSFR than the SF sample due to the much higher percentages in the 1σ–2σ and 2σ–3σ below regions. BAT AGN occur in the 1σ–2σ region at a >3 times higher rate than the CGS and more than two times in the 2σ–3σ below region. Further 64 per cent of the CGS occur inside the MS compared to only 40 per cent of the BAT AGN. So over the entire population, AGN are more likely to be found in host galaxies that have lower SFRs than the MS.

5.2 Differences between Seyfert 1s and 2s

According to the unified model (Antonucci 1993; Urry & Padovani 1995), orientation distorts our view of AGN and causes the differences seen between Sy 1s and 2s. Current models invoke an anisotropic dusty and possibly clumpy torus (e.g. Nenkova et al. 2008; Hönig & Kishimoto 2010) that absorbs and scatters the nuclear optical/UV/X-ray emission. Two regions of ionized gas produce optical emission lines, one at relatively close distances to the central AGN that produces broad emission lines (i.e. broad-line region, BLR) and one at further distances that produces narrow emission lines (i.e. narrow-line region, NLR). Under the unified model, Sy 1 galaxies, which display very bright nuclear point sources as well as broad optical emission lines, are viewed along lines of sight through the opening angle of the torus allowing access to the BLR and accretion disc. Sy 2 galaxies on the other hand display weaker or

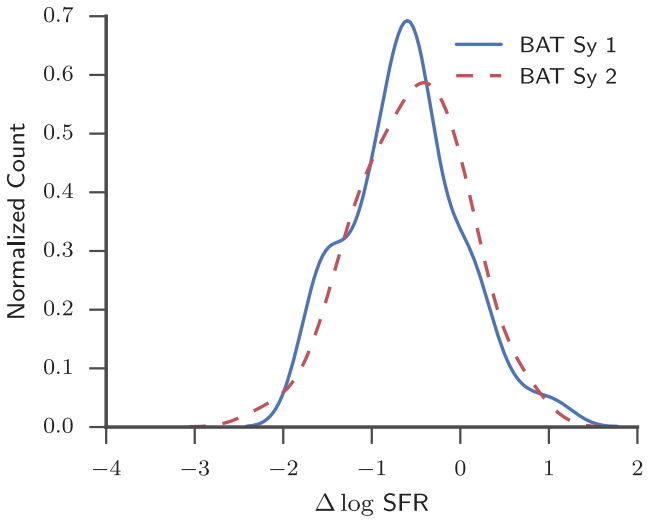

Figure 4. KDE of Δlog SFR for Sy 1s (solid blue line) and Sy 2s (dashed red line) showing the similarity between the two. A colour version of this figure is available online.

even absent central point sources and only narrow emission lines are viewed through the dusty torus that only allows access to the NLR and obscures emission from the BLR and accretion disc. However, assuming that orientation is the only difference means Sy 1s and Sy 2s should display virtually the same host galaxy properties since the torus only affects the very central regions and not the galaxy-wide properties. With our focus on the MS, this means Sy 1s and Sy 2s should not separate out in Fig. 1.

Indeed, both Fig. 1 and Table 1 suggest that this is the case. Sy 1s compared to Sy 2s in each region show a per cent difference of +1, +10, −9, −3, and −0 per cent. Assuming Poisson statistics, these differences are all well within the 1σ error bars. Only the 10 and 9 per cent differences for the inside the MS and 1σ–2σ regions have a marginal 1σ significance.

To investigate further, we compared the Δ log SFR distribution for both Sy 1s and Sy 2s, and Fig. 4 displays their histograms. Apart from the increased absolute numbers of Sy 2s, Sy 1s and Sy 2s have similar distributions of Δ log SFR. Using a K-S test to test whether they are drawn from the same parent population, we find a p-value of 0.36, again indicating that Sy 1s and Sy 2s are similar in terms of their Δ log SFR. This is in agreement with Koss et al. (2010) who found no difference in $u-r$ colours between broad- and narrow-line AGN. This is in disagreement with previous studies (e.g. Heckman et al. 1989; Maiolino et al. 1995; Buchanan et al. 2006) that found Sy 2s reside in more highly star-forming galaxies. However, these samples and conclusions are based on smaller samples as well as different selection criteria. Samples selected using optical or MIR emission will inherently be influenced by the level of star formation in the host galaxy and bias samples towards higher SF objects, especially for Sy 2s that are fainter at these wavelengths due to obscuration.

5.3 Correlation of Δ log SFR with host galaxy and AGN properties

Given the large percentage of AGN host galaxies below the MS compared with normal, MS galaxies, we examined the relationship between Δ log SFR and various AGN and host galaxy properties. Because our entire sample consists of AGN, the immediate reaction is to assume that the AGN has influenced star formation in the host galaxy through some mechanism and slowed it down. From this scenario, the expectation is for more powerful AGN to have a greater effect on the host galaxy and occur further from the MS. To test this, we binned the sample according to the regions described in Section 5.1. Within each bin we calculated the mean 14–195 keV luminosity ($L_{\rm X}$) since Winter et al. 2012 found the 14–195 keV luminosity to be a very good probe of the overall bolometric luminosity and strength of the AGN.

The top-left plot of Fig. 5 shows the resulting relationship between Δ log SFR and $L_{\rm X}$. We found no clear correlation between the strength of the AGN and Δ log SFR. Over the entire range of Δ log SFR, the mean $L_{\rm X}$ only changes by <0.4 dex with a large spread in each region. We calculated the Spearman rank correlation coefficient ($\rho_{\rm s}$) and used bootstrap analysis to determine the 95 per cent confidence interval. We found $\rho_{\rm s}=-0.1$ with a 95 per cent confidence interval of −0.3 to 0.1 consistent with $\rho_{\rm s}=0$. This would seem to argue against the AGN having any effect on star formation in the host galaxy. However, Hickox et al. (2014) argue that AGN variability will smear out any intrinsic correlations between star formation and AGN activity due to the much shorter time-scales of AGN activity compared to star formation. The ultra-hard X-rays used to calculate the luminosity for the BAT AGN presumedly originate very near the SMBH and represent an instantaneous strength while the SFRs are averaged over ∼100 Myr. The null correlation and large scatter we see between $L_{\rm X}$ and Δ log SFR then are most likely a product of the large variability that AGN typically exhibit.

The middle plot indicates that there is a positive correlation between $L_{\rm Grey}/L_{\rm MIR}$ and Δ log SFR. $L_{\rm Grey}/L_{\rm MIR}$ is the ratio of the luminosity of the greybody component to the luminosity of the MIR power-law component used in our SED model. The MIR power-law luminosity strongly correlates with the AGN luminosity (Shimizu et al., in preparation) and is assumed to be produced by the AGN, while the greybody luminosity is assumed to be a product of star formation. The ratio of their luminosities is a measure of which component dominates the SED. Far below the MS, the IR SED should be dominated by the AGN, while the IR SEDs of MS galaxies as well as those above the MS are dominated by star formation. We expect this trend due to the null correlation of $L_{\rm X}$ with Δ log SFR. Since $L_{\rm MIR}$ is strongly correlated with $L_{\rm X}$, a decrease in Δ log SFR is then mostly due to a decrease in SFR which was directly calculated from $L_{\rm grey}$. We again calculated $\rho_{\rm s}$ finding $\rho_{\rm s}=0.6$ [0.46–0.7] where the range in brackets is the 95 per cent confidence interval determined using a bootstrap analysis. This strongly suggests a real positive correlation between $L_{\rm Grey}/L_{\rm MIR}$ and Δ log SFR and confirms that far below the MS the IR SED is most likely dominated by the AGN.

The greybody dust temperature also suggests a positive correlation with Δ log SFR with galaxies at larger Δ log SFR having a higher temperature (Fig. 5, right). This has been observed before (e.g. Magnelli et al. 2014) and can easily be explained given that an increase in SFR increases the number of OB stars that produce the UV photons to heat the dust. We found $\rho_{\rm s}=0.6$ [0.45–0.7], very similar to the correlation with $L_{\rm Grey}/L_{\rm MIR}$ showing that the true property determining an AGN host galaxy's location within the MS diagram is star formation rather than the strength of the AGN.

Both of these effects can also be seen in Fig. 6 where we plot the mean SEDs for each region after normalizing to the 12 μm flux density. Because some of the observed SEDs contain upper limits especially at the longest wavelengths, we use the Kaplan–Meier product-limit estimator (Feigelson & Nelson 1985), a maximum likelihood estimate of the distribution function, to calculate the mean and its standard error. Using only the detected flux densities would bias the mean towards larger values, with an

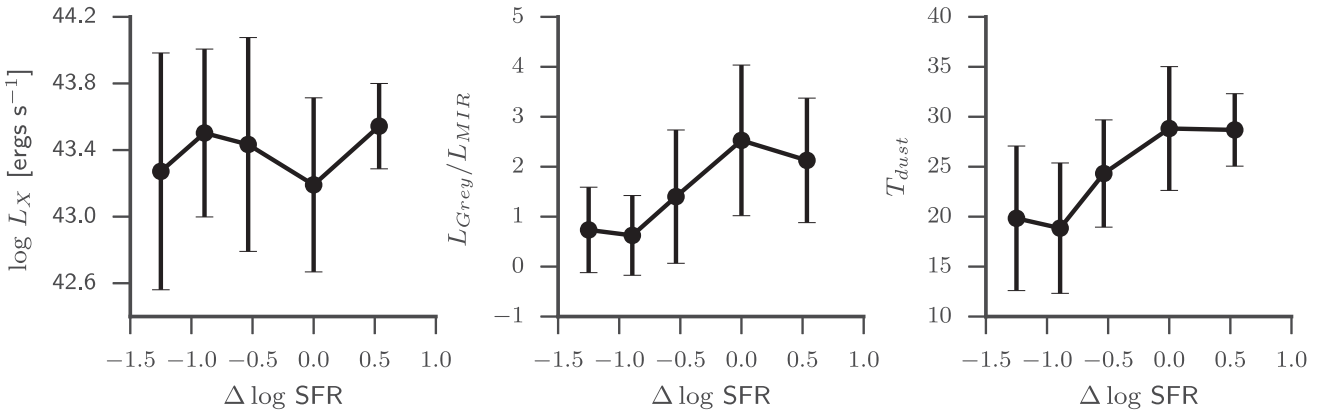

Figure 5. Correlations between different properties of the galaxies/AGN as a function of Δ log SFR. Left: 14–195 keV luminosity, Middle: ratio of the MIR power-law luminosity to greybody luminosity. Right: dust temperature. For each property, we binned the sources according to whether they were above, inside, or below the MS (split into three separate regions). For each MS region, we calculated the mean AGN/galaxy property. Error bars are the standard deviation within each bin.

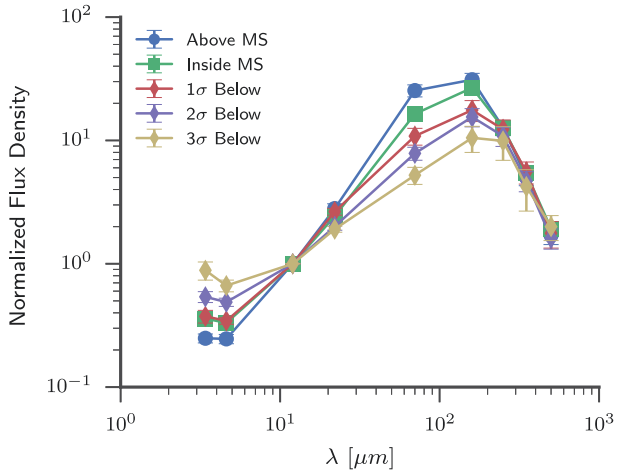

Figure 6. Mean SED of the sources in each region of the MS plot. The individual SEDs were first normalized to the 12 μm flux density. Error bars represent the standard error of the mean normalized flux. A colour version of this figure is available online.

increasing bias at longer wavelengths as the number of upper limits increases. This would then lead to an artificial flattening of the SED.

The peak of the SED is seen to shift to longer wavelengths as sSFR decreases, indicating colder temperatures (i.e. Wien's displacement law), while the overall amplitude decreases along with a flattening of the slope of the SED between 4.6 and 160 μm. In their analysis of *Spitzer* IRS spectra for Seyfert galaxies, both Wu et al. (2009) and Baum et al. (2010) found that AGN host galaxies with lower amounts of star formation display bluer SEDs in 15–40 μm regime, in agreement with our mean SEDs and an increase in the AGN contribution. We also see a general increase in the *W1*/*W2* *WISE* colour moving towards lower sSFR, an indication that the host galaxy (in particular older stars) begins to contribute to the MIR, similar to what is observed in many quenched galaxies. The long-wavelength IR regime, though, seems to be completely unaffected by the sSFR. All five of the SEDs essentially display the same slope and relative flux density at 250, 350, and 500 μm. Indeed, a comparison of the BAT AGN SPIRE colours with the HRS colours shows that there is little difference between the two samples (Shimizu et al., in preparation), verifying that the same process (i.e. star formation) is producing most of the long-wavelength emission.

5.4 Host galaxy morphology

Koss et al. (2011) closely analysed the host galaxy morphologies of the BAT AGN, finding that at all stellar masses a larger percentage of AGN are hosted by spiral galaxies compared to a matched sample of normal galaxies. Using these morphologies, we can assess if we observe a change in the host galaxy morphology as a function of sSFR. Koss et al. (2011) classified the BAT AGN into three categories: spirals, ellipticals, and intermediate based on the results from the Galaxy Zoo project (Lintott et al. 2008). Each galaxy was independently classified numerous times by the public. A spiral or elliptical morphology was chosen for the galaxy if >80 per cent people selected the type, or else intermediate was chosen. Mergers were defined in the same way as Patton & Atfield (2008) and Koss et al. (2010), requiring a projected distance of at most 30 kpc and a radial velocity difference of <500 km s^{-1} between the galaxy and its companion. We used the same method for the COLD GASS sample as for the spiral/elliptical/intermediate classification. Merger classifications for the COLD GASS sample were determined in Saintonge et al. (2012) where they visually classified each galaxy as a merger/interaction if it had a nearby companion (<1 arcmin) and/or evidence of a disturbed morphology, tidal tails, etc. (see appendix A of Saintonge et al. 2012). Each galaxy that looked like a merger was given a merger rating from 2 to 5 with 2 representing galaxies that only had a nearby companion and a 5 representing galaxies with very strong signs of a merger. After looking through the images of the COLD GASS mergers, we decided to exclude all of the galaxies with a merger rating of 2 because they would not have been classified as a merger using the method from Koss et al. (2011). We chose to only compare the BAT AGN morphologies with the COLD GASS sample given COLD GASS's better mass completeness and larger SFR depth.

In the 'Total' column of Table 2 and Fig. 7, we outline the total fraction of galaxies that are spirals, intermediates, and ellipticals over the whole sample. Spiral galaxies dominate (∼60 per cent) the population of both the BAT AGN and CGS similar to what was found in Koss et al. (2011) whereas for the CGA they represent ∼50 per cent of the population and for the CGL they are 35 per cent. There are virtually no spiral galaxies in the quiescent group (CGQ).

Table 2. Host galaxy morphology distribution in the SFR–M_* plane.

Sample (1)	Total (2)	Above MS (3)	Inside MS (4)	1σ–2σ below (5)	2σ–3σ below (6)	$>3\sigma$ below (7)
BAT AGN						
Spirals	0.64	0.06	0.33	0.26	0.21	0.14
Ellipticals	0.10	0.00	0.18	0.18	0.09	0.55
Intermediates	0.17	0.05	0.11	0.42	0.16	0.26
Mergers	0.28	0.09	0.34	0.28	0.22	0.06
CG All						
Spirals	0.43	0.03	0.52	0.20	0.12	0.13
Ellipticals	0.23	0.00	0.03	0.03	0.08	0.86
Intermediates	0.34	0.03	0.28	0.16	0.13	0.41
Mergers	0.02	0.41	0.40	0.00	0.19	0.00
CGS						
Spirals	0.59	0.04	0.74	0.16	0.04	0.03
Ellipticals	0.11	0.00	0.06	0.00	0.11	0.84
Intermediates	0.29	0.06	0.60	0.11	0.07	0.18
Mergers	0.03	0.34	0.66	0.00	0.00	0.00
CGA						
Spirals	0.48	0.02	0.34	0.25	0.14	0.25
Ellipticals	0.18	0.00	0.08	0.06	0.14	0.72
Intermediates	0.35	0.02	0.29	0.28	0.15	0.26
Mergers	0.03	0.49	0.01	0.00	0.50	0.00
CGL						
Spirals	0.35	0.00	0.21	0.27	0.26	0.27
Ellipticals	0.26	0.00	0.00	0.08	0.17	0.76
Intermediates	0.39	0.00	0.00	0.18	0.30	0.53
Mergers	0.00	0.00	0.00	0.00	0.00	0.00
CGQ						
Spirals	0.03	0.00	0.00	0.00	1.00	0.00
Ellipticals	0.59	0.00	0.00	0.00	0.00	1.00
Intermediates	0.38	0.00	0.00	0.00	0.00	1.00
Mergers	0.00	0.00	0.00	0.00	0.00	0.00

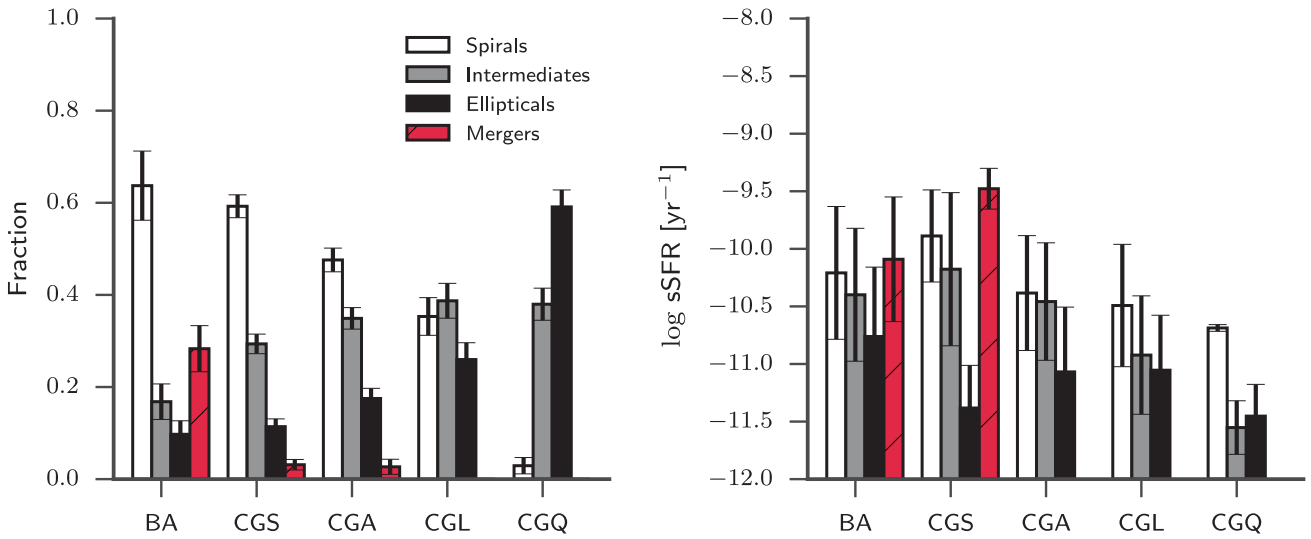

Figure 7. Left: the distribution of spirals, intermediates, and ellipticals for all of the galaxy samples. For the COLD GASS samples, the fractions represent the mean fraction of all 50 representative subsamples. 1σ error bars for the BAT AGN (BA) were calculated assuming Poisson statistics while the error bars for the COLD GASS samples represent the standard deviation of the fractions for the 50 representative subsamples. Right: the average sSFR for the different morphologies within each sample. For the COLD GASS samples, we randomly chose one representative subsample which for the CGA in this case did not contain any mergers. Error bars are the standard deviation of sSFR within each group. A colour version of this figure is available online.

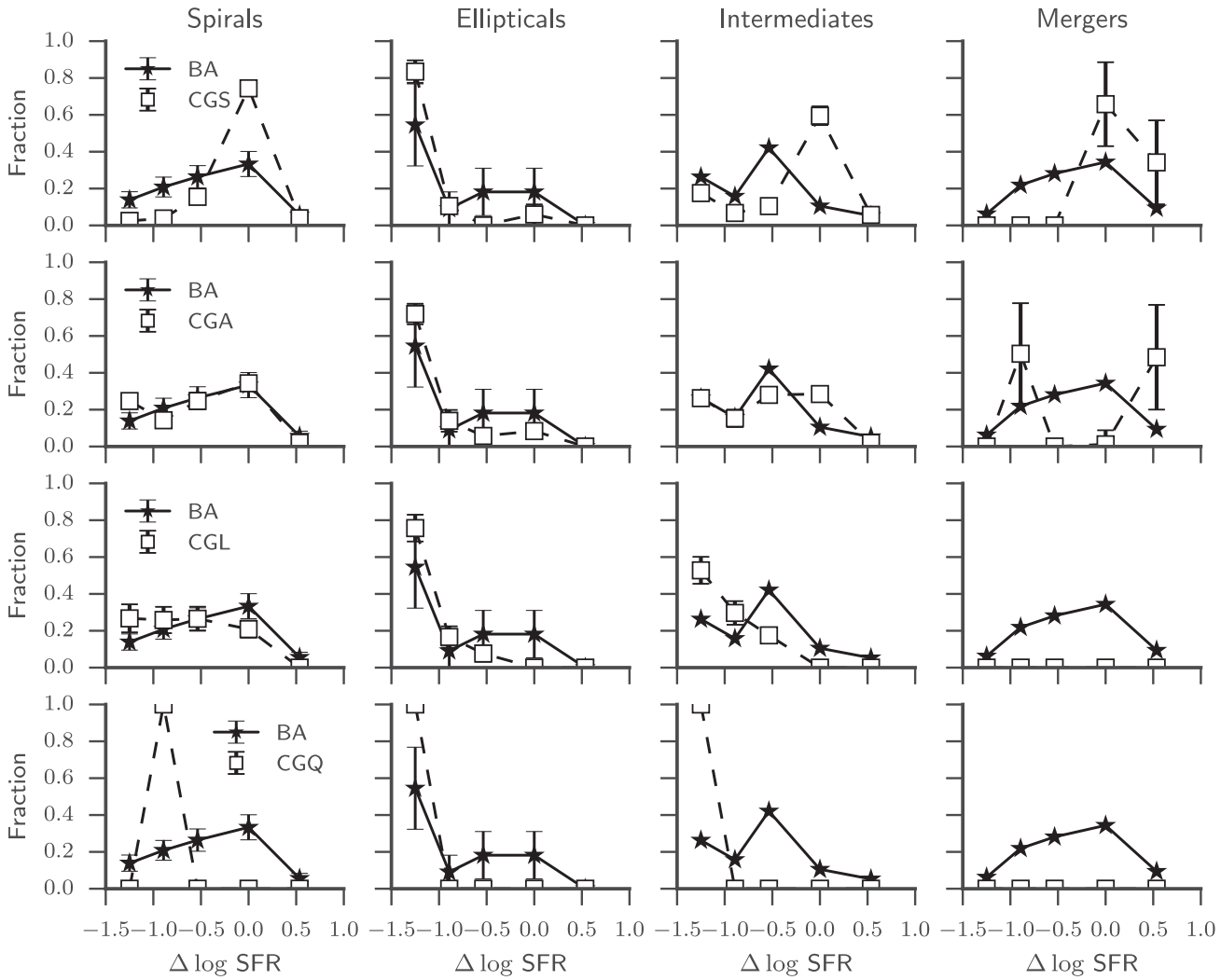

Figure 8. Comparison of the fraction of spirals, ellipticals, intermediates, and mergers that are in each MS region for the BAT AGN (BA) and COLD GASS samples (CGS, CGA, CGL, and CGQ). The fractions for the COLD GASS samples are the average fractions over the 50 representative subsamples. Errors for the BAT AGN are calculated assuming Poisson statistics while the errors for the COLD GASS samples are the standard deviation of the fraction for the 50 representative subsamples.

On the other hand, the CGQ are dominated by elliptical galaxies (∼60 per cent). The CGL are ∼26 per cent elliptical, CGA 20 per cent, and the BAT AGN and CGS 10 per cent elliptical. Overall in terms of the whole population, the BAT AGN more closely resemble the morphology distribution of the CGS rather than the CGA. However, a closer look at the sSFR for each morphology shows that the BAT AGN and CGA are more similar. This is shown in Fig. 7 (right-hand panel) where we plot the average sSFR for each morphology. BAT AGN spirals and intermediates show decreased levels of sSFR compared to the CGS and more in line with the CGA. If we examine the distribution of spirals, ellipticals, and intermediates as shown in Fig. 8, we can again see that the BAT AGN and CGA are almost identical in terms of the fraction of spirals and ellipticals in each MS region. The biggest difference seems to occur with intermediates; however, there is much uncertainty concerning the nature of intermediates given that they are simply defined as objects where there was no consensus on whether it was a spiral or elliptical.

Interestingly for both the BAT AGN and CGA, ellipticals show increased levels of sSFR compared to those within the CGS and CGQ groups. This could be an indication that AGN within early-type galaxies actually stimulate star formation rather than quenching it. With such large error bars, though, the significance of this result is unclear.

In agreement with Koss et al. (2010), we find that the merger fraction of the BAT AGN (28 per cent) is much higher than that of the CGS (3 per cent) and CGA (3 per cent). There are no mergers in the CGL and CGQ samples. Mergers have long been known to increase the SFR in the interacting galaxies (Sanders et al. 1988) as evidenced by the majority of ULIRGS involved in one. Elbaz et al. (2011) found that nearly all of the local galaxies above the MS are IR-compact starbursts that were most likely triggered by a merger. Thus, we expect to see a large fraction of mergers occurring above the MS. Indeed, this is the case especially for the CGS where 34 per cent of the mergers are above the MS and the rest are inside the MS. Further for both the BAT AGN and CGS, mergers have the greatest average sSFR (Fig. 7). This could also explain the extremely low merger fraction for the CGA. If mergers are associated with highly star-forming galaxies, then emission line ratios would indicate an SF galaxy rather than an AGN as any AGN

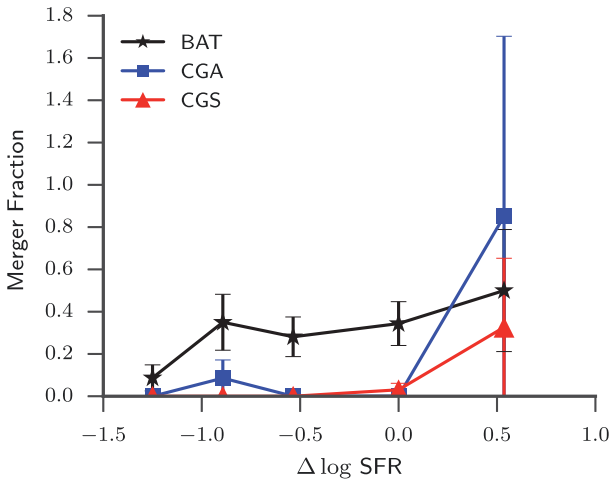

Figure 9. Fraction of galaxies in each MS region that are mergers for the different samples. Errors for the BAT AGN (black stars) are calculated assuming Poisson statistics for the merger fraction. Errors for the CGA (blue squares) and CGS (red triangles) are the standard deviation of the fraction over all 50 representative subsamples. A colour version of this figure is available online.

signatures would be overwhelmed. With ultra-hard X-rays though, we can peer through the obscuring gas and detect the AGN.

In Fig. 9, we plot the fraction of all galaxies of a sample in an MS region that is a merger. This is different from Fig. 8, where we plot the fraction of all mergers that are present in each region. Here we can see that the merger incidence rate rises with $\Delta \log$ SFR as expected. Above the MS, the CGA show the highest merger rate at roughly 80 per cent, but this is based on small number statistics and is reflected in the large error bars. The BAT AGN have a 50 per cent merger rate and CGS are at 30 per cent. For all three samples, the 'above the MS' region represents the largest merger rate. Inside, and below the MS the BAT AGN clearly show much larger merger rates than that of CGS and CGA. In fact, the merger fraction for the BAT AGN is roughly flat from above the MS to the 2σ–3σ region. This could be evidence that mergers and interactions are important in triggering AGN at low redshift even before the starburst ignites and those below the MS are in fact moving up the SFR–M_* plane. Another explanation is that these are late-stage mergers and have moved past the initial burst of star formation and are slowly falling off the MS. A confirmation of this would be if all of the mergers in the $>1\sigma$ region are in the early stages whereas the ones above the MS are near coalescence. In either case, the BAT AGN mergers occur across nearly the whole SFR–M_* plane at a high rate compared to local non-active galaxies and optically selected AGN. This is in disagreement with recent higher redshift studies of the merger rate in X-ray selected galaxies (e.g. Kocevski et al. 2012; Villforth et al. 2014) that find no difference in the merger rates between AGN and non-AGN galaxies.

6 DISCUSSION

6.1 Selection effects and model dependence

Due to the flux-limited nature of our parent AGN sample, there is a strong dependence on the X-ray luminosity (i.e. AGN luminosity) with distance, limiting the inclusion of low-luminosity AGN especially at higher redshifts. However, this would only affect our results if they were related to either the SFR or M_* of the host galaxy. X-ray luminosity has been shown to only have a weak correlation with SFR (e.g. Silverman et al. 2009; Shao et al. 2010; Mullaney et al. 2012a; Rosario et al. 2012). Furthermore, the correlations are positive implying that the absence of low AGN luminosity in our sample only removes objects with even lower SFR that would enhance our result that a large fraction of AGN lie below the MS. Mullaney et al. (2012a) found a very weak correlation of intrinsic AGN luminosity with stellar mass where a two-order increase in AGN luminosity results in only a factor of 2 greater stellar mass. This combined with the weak correlation of SFR shows that we are not biased towards low-sSFR galaxies in our sample.

The choice of model to fit the SEDs of our galaxies could greatly influence the results, given that the SFRs are directly calculated from the measured FIR luminosity. It is possible that we are assigning too much of the 8–1000 μm luminosity to the AGN and underestimating the SFR. We have tested this effect in two ways. First, we implemented the SED-fitting routine, DECOMPIR, described and developed by Mullaney et al. (2011). DECOMPIR utilizes a set of five host galaxy templates and an intrinsic AGN template to fit the IR SEDs of galaxies. Although there is the option to let the parameters of the AGN template vary, given our sample, we only used the mean intrinsic AGN SED found in Mullaney et al. (2011). Each BAT AGN was fitted with each host galaxy template allowing the normalizations of both the AGN and host galaxy to vary. The host galaxy template that resulted in the minimum χ^2 was chosen as the best fit. SFRs were then calculated by integrating the best-fitting host galaxy SED from 8 to 1000 μm and using equation (1). Using the DECOMPIR SFRs combined with the same stellar masses and MS relation (defined by equation 3), we find 6, 35, 28, 14, and 18 per cent of the AGN in the above MS, inside MS, 1σ–2σ below, 2σ–3σ below, and $>3\sigma$ below regions, respectively. These fractions are extremely similar to those using the Casey 2012 model (Table 1) with only a slightly higher incidence of AGN inside the MS and lower number below it.

The second way we tested the model dependence was by using just the monochromatic 160 μm luminosity as a pure SFR indicator. The 60 or 70 μm luminosity has been used extensively in the literature as an SFR indicator; however, based on the modelling of the BAT sample, 70 μm is a poor choice due to the AGN contribution especially at higher AGN luminosities (Meléndez et al. 2014). 160 μm however seems to be relatively free from any AGN contribution. Therefore, we simply used the 160 μm luminosity to convert to an SFR using the relation from Calzetti et al. (2010) for both the HRS sample and BAT AGN and recalculated the MS based only on the HRS since we do not have 160 μm data for the HerS sample. This results in 6, 37, 25, 12, and 20 per cent of the BAT AGN in the above MS, inside MS, 1σ–2σ below, 2σ–3σ below, and $>3\sigma$ below regions, respectively, comparable to both the values in Table 1 and using DECOMPIR. This confirms our main result that a large fraction of AGN lie below the MS and is not a product of oversubtracting the AGN component of the SED. Three separate techniques for estimating the SFR agree that >50 per cent of AGN have lower sSFRs than normal galaxies for the same stellar mass.

6.2 Comparison with previous studies

We have substantiated that our results are not due to selection effects or are model dependent. The BAT AGN, COLD GASS AGN, and HerS AGN span a large range in sSFR that extends over two orders of magnitude. Many previous studies have suffered from low detection rates (<40 per cent) in the FIR and needed to resort to stacking techniques (e.g. Mullaney et al. 2012a) to achieve a reasonable

dynamic range. Our *Herschel*-BAT AGN sample provides a unique opportunity to compare to previous work and whether assumptions made remain valid. In particular, we will focus on the work from Mullaney et al. (2012a) who used deep *Herschel* observations of the GOODS-South and GOODS-North fields to study the SF properties of AGN selected from 2 and 4 Ms *Chandra Deep Field*-South and North. Their AGN sample spans the same luminosity range as the BAT AGN, but a much higher redshift range ($0.5 < z < 3$) with an overall detection fraction in the FIR of ∼40 per cent. To enhance their sample to low redshifts, they utilize a sample of the BAT AGN, however with much poorer FIR photometry from *IRAS* and again only a detection fraction of 40 per cent compared to our 95 and 83 per cent detection fraction at 70 and 160 μm, respectively, the two wavelength bands closest to the longest *IRAS* bands.

For the FIR undetected AGN in the GOODS fields, they utilized stacking analysis to find the weighted average sSFR in three different redshift bins. Using a Monte Carlo approach and assuming a lognormal distribution of sSFR, they estimated that 15 per cent of all (FIR detected and undetected) AGN reside in quenched galaxies, 79 per cent are in MS galaxies, and 7 per cent in starburst galaxies. While the starburst percentage (i.e. above the MS) is comparable to the fraction presented here, the MS and quenched (i.e. below the MS) percentages seem to be in disagreement. However, this is merely due to a difference in definition of being inside or below the MS. Mullaney et al. (2012a) define starbursts as galaxies that have sSFRs >3 times that of MS galaxies and quenched galaxies as ones that have 10 per cent the sSFR of MS galaxies. All others are then considered normal SF galaxies which include transitioning galaxies in the 'green valley'. Using these criteria for our BAT sample, we then find 14 per cent starburst galaxies, 73 per cent MS galaxies, and 13 per cent quenched galaxies. While we seem to see a factor of 2 greater incidence of starburst galaxies, the fractions of MS galaxies and quenched galaxies are completely in line with Mullaney et al. (2012a).

To further check the agreement between the two studies, we simulated samples of AGN at higher redshifts by assuming that our BAT AGN sample is representative of the AGN population at all redshifts. To simplify the process, we also assumed that every AGN has a host galaxy SED exactly that of the SB5 template from DECOMPIR at $z = 0$. The template was then scaled to have the same observed 160 μm flux. For each redshift bin probed by Mullaney et al. (2012a) (0.5–1.0, 1–2, and 2–3), we simulated 1000 samples of AGN by randomly assigning a redshift from that bin to each of the AGN in our BAT sample. After a redshift was assigned, we simulated the increase in SFR with increasing redshift using equation 13 from Elbaz et al. (2011). From this, we obtained a multiplicative factor to boost the IR SED of the AGN for a specific redshift. Finally, after redshifting the SED, we employed the same detection wavelengths (100 μm for $0.5 < z < 1.5$ and 160 μm for $1.5 < z < 3.0$) and thresholds (0.8 mJy for 100 μm and 2.4 mJy for 160 μm) to determine whether the source would be detected. The detection fractions for all 1000 sets of AGN were averaged to find the estimated detection fraction for each redshift bin.

Overall for the entire redshift range of 0.5–3, we found a detection fraction of ∼35 per cent, very near to the observed one of 42 per cent. However, when splitting up into the redshift bins, we find detection fractions of 71, 30, and 6 per cent compared to 60, 42, and 29 per cent found by Mullaney et al. (2012a) in redshift bins of 0.5–1.0, 1–2, and 2–3, respectively. This could be a sign of an evolution of AGN host galaxies where at higher redshifts, more AGN live in MS galaxies than what is seen at low redshift. The discrepancy could also be caused by the lack of an AGN contribution used in our simulations. At 100 and 160 μm, there is very little contamination from the AGN, but at the rest-frame wavelengths being probed (40–67 μm) it could have a profound effect. To test this, we repeated the simulations, adding in the average AGN SED from DECOMPIR such that 25 per cent of the observed-frame 100 or 160 μm is due to the AGN. Doing this increases the detection fraction to 77, 38, and 10 per cent in the same redshift bins, much closer in the middle bin but still far off the 30 per cent in the highest redshift bin. However, we have not included any AGN luminosity evolution with redshift. Ueda et al. (2014) find that L_X is a strong function of redshift especially between $z = 0$ and 2. This would increase the fluxes especially in the higher redshift bins and subsequently increase the detection fractions.

6.3 Comparison with SDSS sample

All three AGN samples, one X-ray selected (BAT AGN) and two optically selected (CGA and HerS AGN), have reduced levels of star formation compared to the MS. All of these samples, however, are relatively small in number so we decided to test a much larger sample of both SF and AGN galaxies from the SDSS.

The SDSS DR7 spectroscopic catalogue mentioned previously contains 818 333 unique galaxies with optical spectra that were analysed in a consistent manner by the MPA-JHU team (Brinchmann et al. 2004). SFRs and stellar masses were measured for every galaxy. Stellar masses are based on fits to the five SDSS photometry using the technique described in Salim et al. (2007). SFRs were derived in two separate ways. For SF galaxies, the SDSS spectra were fitted using the Charlot & Longhetti (2001) models with an additional aperture correction to account for light outside the fibre (Salim et al. 2007). For the other classifications, emission lines are not reliable either due to low S/N or unknown AGN contribution (composite and AGN dominated). The SFRs for these groups were estimated using the 4000 Å break (D_n4000) which has been shown to correlate with sSFR, albeit with large scatter (Brinchmann et al. 2004).

We restricted the SDSS sample to only those galaxies with well-measured redshifts ($z_{conf} > 0.9$) and in the redshift range $0.01 < z < 0.05$. The upper limit matches the upper redshift of our BAT AGN sample and the lower limit is to avoid very nearby galaxies that the SDSS pipeline can shred into multiple sources. We further included an absolute magnitude cut of $M_z < -19.5$ to ensure mass completeness and only used galaxies with well-measured SFRs (sfr_flag = 0). These restrictions resulted in 21 091 SF galaxies, 8189 low-SFR galaxies, 12 190 composite, and 9421 AGN-dominated systems. We combined the SF and low-SFR galaxies to form the SDSS normal galaxy sample. Fig. 10 shows the distribution of sSFR for the SDSS normal galaxies. There is a clear bimodality in sSFR that matches the bimodality seen with optical colours and in the COLD GASS sample. The threshold between the two populations occurs at sSFR $\sim 10^{-11}$ yr^{-1} shown by the vertical dashed line. We use this threshold to split the SDSS normal galaxy sample into an actively star-forming population and passive population, hereafter referred to as $SDSS_{SF}$ and $SDSS_{passive}$.

In Fig. 11, we plot the number density of the SDSS galaxies on the SFR–M_* diagram separated into the various classifications. In the left-hand panel of Fig. 11, we plot the $SDSS_{SF}$ galaxies (blue contours) along with the $SDSS_{passive}$ galaxies. The black solid line is the MS relation found by Peng et al. (2010) using the same data while the dashed line corresponds to a constant sSFR $=10^{-11}$ yr^{-1}. The $SDSS_{SF}$ galaxies follow the Peng et al. (2010) MS relation just as the HRS galaxies follow their own MS relation with the passive

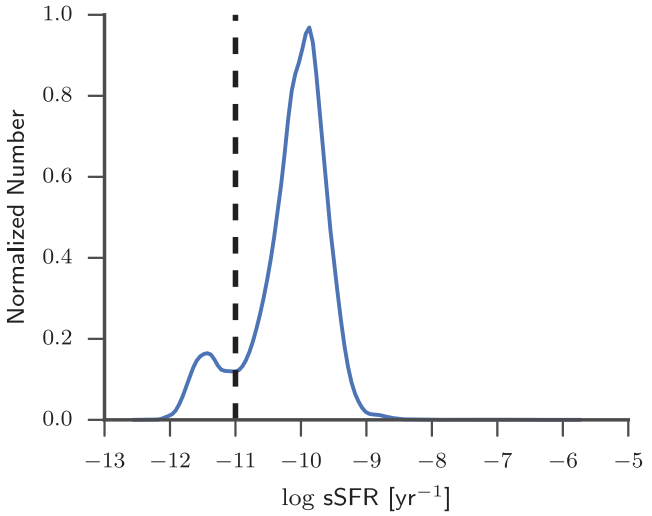

Figure 10. KDE of the sSFR for the SDSS DR7 sample. There is a clear bimodality in sSFR defining the two populations of actively star-forming and passive galaxies with a transition around 10^{-11} yr^{-1} (dashed line). A colour version of this figure is available online.

galaxies far below. In the right-hand panel of Fig. 11, we plot the SDSS composite (magenta contours) and AGN-dominated galaxies (green contours). The same effect is seen as when comparing the BAT AGN, CGA, and HerS AGN with the MS, CGS, and HerS SF. AGN host galaxies systematically have lower rates of star formation than normal SF galaxies. SDSS AGN and composites, BAT AGN, CGA, and HerS AGN definitively lie in between the actively star-forming and completely quenched population signalling that these galaxies are possibly transitioning from one stage to the next.

6.4 Implications for galaxy evolution and AGN feedback

In this paper, we have rigorously shown that Seyfert galaxies display lower levels of star formation than that expected from the MS by comparing normal galaxy samples with an ultra-hard X-ray selected AGN sample using the same methods for measuring the SFR and stellar mass. Optically selected AGN from the COLD GASS and HerS sample also show the same effect even though their SFRs were measured using a different method. Extending the comparison to large numbers with the SDSS further emphasizes the difference between AGN and non-AGN galaxies and confirms our results with the much smaller samples.

Just because AGN host galaxies have systematically lower sSFRs than non-AGN galaxies however does not directly imply that AGN feedback is taking place. Two scenarios can possibly explain our results. (1) AGN actively quench star formation through short outbursts during the late life of the galaxy. (2) AGN are simply the result of the availability of cold gas in a galaxy.

High-mass SF galaxies on the MS are gas rich especially in molecular gas (Saintonge et al. 2012). This large cold gas supply can fuel both star formation and AGN activity. If we prescribe to the 'bathtub' model of gas regulation (Lilly et al. 2013), the SFR is simply proportional to the mass of the gas reservoir in the galaxy. The two processes that regulate the mass are the accretion rate from the halo and a wind outflow, which in Lilly et al. (2013) is proportional to the SFR.

In the first scenario, we can imagine the AGN significantly adding to the decrease of gas mass in the galaxy through several ways such as halo heating and powerful winds. All of these feedback processes work to reduce the mass of gas in the galaxy, which then reduces the SFR and produces the shift in sSFR we see compared to non-AGN SF galaxies (Fig. 3). However, based on Fig. 5 we know that the SFR is not connected to the *instantaneous* AGN strength, rather the SFR is correlated with the *average* AGN strength over 100 Myr timescales (Chen et al. 2013). So if AGN feedback is working, it must be only over relatively short periods of time probably while undergoing a powerful outburst. This is supported by findings of molecular outflows in powerful AGN (Veilleux et al. 2013; Cicone et al. 2014) where the mass outflow rate was shown to rise with increasing AGN luminosity. It is also supported by the discovery of 'voorwerpje' (Lintott et al. 2009; Keel et al. 2012, 2015), highly ionized clouds

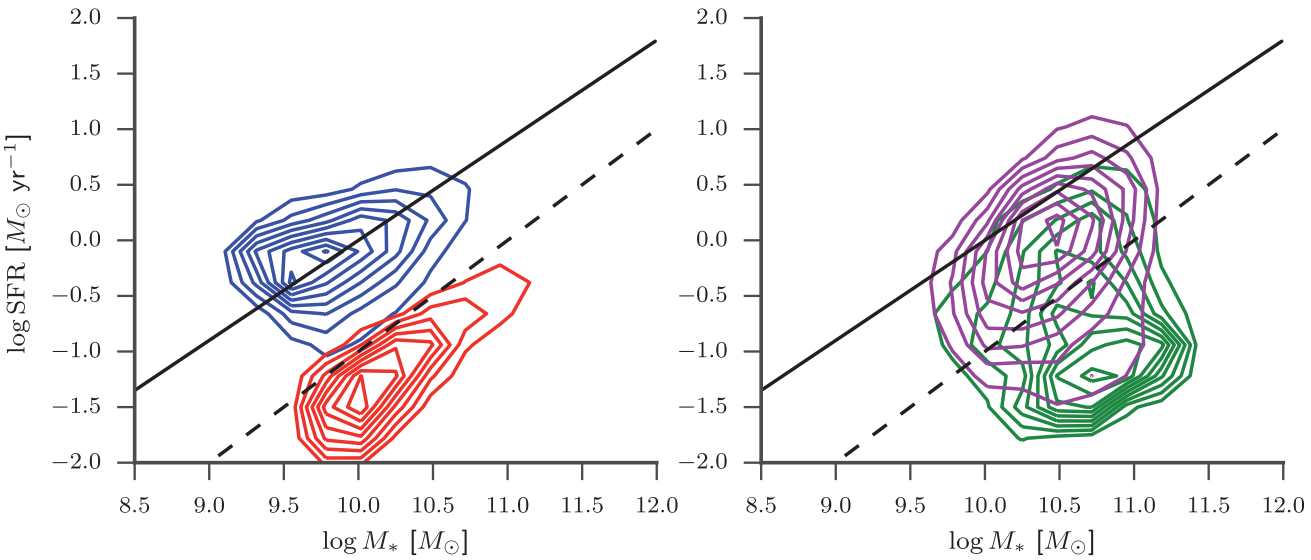

Figure 11. SFR–M_* diagram for the spectroscopic SDSS DR7 sample. Left-hand panel: SDSS non-AGN galaxies split into 'SF' (blue contours) and 'passive' (red contours) based on the sSFR. The black line indicates the sSFR = 10^{-11} yr^{-1} threshold to split the sample into 'active' and 'passive'. Right-hand panel: same as the left-hand panel with contours representing the SDSS composite (magenta contours) and AGN-dominated galaxies (green contours). Contours enclose 10–90 per cent of the specified sample in increments of 10 per cent. A colour version of this figure is available online.

at kpc scales around currently dormant SMBH that indicate AGN outbursts on time-scales of ∼100 000 yr. Tombesi et al. (2015) recently were able to show that a fast accretion-disc wind is driving a molecular outflow in a ULIRG. Within this framework, this means all of the BAT AGN lying below the MS have gone through at least one powerful phase or possibly more to be able to significantly deplete the galaxy of molecular gas. The AGN still inside the MS perhaps are still waiting for that outburst or have not gone through enough to move off the MS.

In the second scenario, the existence of an AGN is the consequence of the large availability of cold gas in high-mass galaxies. If there is enough cold gas, eventually enough will find its way to the centres to trigger an AGN. AGN would likely turn on while the galaxy is still on the MS. A quenching process unrelated to the AGN, possibly shock heating of the accreting halo gas, slowly shuts down star formation beginning in the outskirts of the galaxy. This would be supported by our findings that the BAT AGN are more compact in the FIR than normal SF galaxies (Mushotzky et al. 2014). The AGN persists as the galaxy falls off the MS, eventually turning off as the remaining cold gas runs out. This scenario is still supported by the findings of Chen et al. (2013). The long time-scale average accretion rate is tightly connected to the SFR through the available gas reservoir. It would only require that gas accretion on to the SMBH not be a smooth and constant process but more intermittent and variable which is supported by high-resolution simulations (Hopkins & Quataert 2010; Novak, Ostriker & Ciotti 2011).

There is one component we are currently ignoring however: mergers and interactions. With 30 per cent of the BAT AGN involved in one, in both scenarios mergers could be the key ingredient for funnelling cold gas to the nuclei of galaxies and igniting an AGN. Schawinski et al. (2014) cite major mergers as the mechanism to cause fast quenching in early-type galaxies whereas late-type galaxies are slowly quenched through a drying up of their gas reservoir. Perhaps both quenching mechanisms are at play in the BAT AGN. The majority are contained in massive spirals (Fig. 7) where AGN feedback (scenario 1) or external processes (scenario 2) are slowly suppressing star formation while the ones involved in a merger have had their SFRs and SMBH accretion rates briefly elevated before rapidly falling off the MS. This could also explain why we still see a large fraction of mergers just below the MS.

Which scenario is dominant is still a matter of debate and at present we are unable to distinguish between these concepts. One thing that is clear though is that massive galaxies go through an AGN phase as they fall off the MS. This is shown in Fig. 12 where we plot the fraction of all galaxies that are classified as an AGN/composite (blue line) or AGN/composite/LINER (magenta line, if we suppose LINERs also contain an AGN) as a function of distance from the MS in the COLD GASS sample. The fractions are the average across all 50 representative subsamples. Both lines peak in the 1σ–2σ and 2σ–3σ below regions with close to 80 per cent of the galaxies in these regions containing an AGN or LINER. The question that remains is whether these AGN have had a substantial effect on the SFR in their host galaxy or they are just 'along for the ride' off the MS. An answer could possibly come from surveys using integral field unit spectroscopy such as MaNGA[9] and CALIFA (Sánchez et al. 2012) that provide spatially resolved spectra across the entire galaxy.

[9] https://www.sdss3.org/future/manga.php

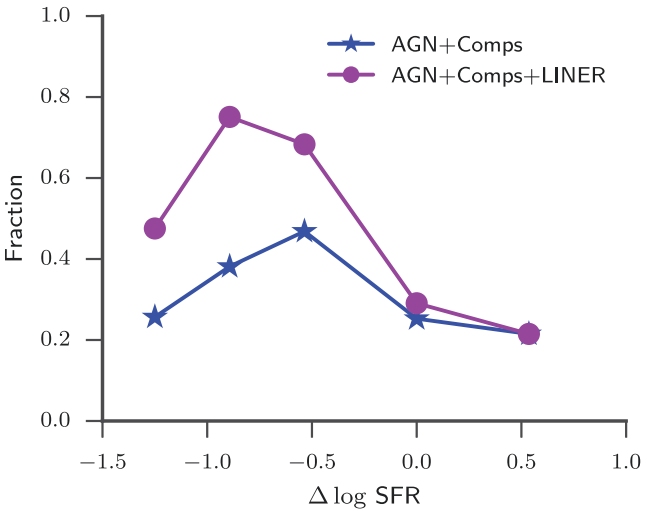

Figure 12. Fraction of all COLD GASS galaxies that are AGN or composite galaxies (blue star) and AGN, composite, or LINERs (magenta circles) as a function of distance from the MS. The fractions shown are the average fractions of all 50 representative subsamples. A colour version of this figure is available online.

7 SUMMARY AND CONCLUSIONS

Using consistent measures of both stellar mass and SFR, we compared three samples of galaxies, a set of local, non-AGN SF galaxies (HRS), a complete set of AGN host galaxies selected from the *Swift*/BAT catalogue, and a mass-selected sample of both SF and AGN host galaxies (COLD GASS). From the HRS, we constructed our own 'MS' relation and systematically analysed the location of the samples with respect to the MS. Our main conclusions are as follows.

(1) AGN host galaxies, both X-ray selected and optically selected, systematically lie below the MS, indicating reduced levels of star formation.

(2) After splitting the AGN sample into regions of increased offset from the MS of star formation, we found no dependence of the offset on hard X-ray luminosity.

(3) Analysing the morphologies of the samples, we find that while the fraction of BAT AGN living in spirals most closely resembles the SF sample, the sSFRs are more closely related to the optically selected AGN. The distribution of sSFR for spirals and ellipticals in the BAT AGN also best matches the distribution for spirals and ellipticals for optically selected AGN. We find a significant increase in the merger fraction from 0.1 well below the MS up to 0.4 near, inside, and above it. The merger fractions for the BAT AGN are much higher than those for the COLD GASS AGN and SF galaxies.

(4) These results are both model independent as well as unaffected by our selection criteria. A detailed comparison with Mullaney et al. (2012a) does not find any discrepancy between the two studies, and evolving our population of AGN to higher redshifts agrees well with their detection fractions.

(5) Expanding the analysis to the larger SDSS sample of galaxies shows that the effect of AGN host galaxies lying below the MS also occurs in larger optically selected samples and confirms the previous findings of AGN preferentially occurring in galaxies in transition from SF to quiescence.

(6) We discussed how the trend in sSFR can be explained by AGN feedback that reduces the supply of cold gas in the galaxy. This

slowly suppresses star formation through short periodic outbursts. It can also be explained if the occurrence of AGN is simply the result of the availability of cold gas. As star formation is quenched through other processes, the AGN follows along and eventually fades as the cold gas runs out. In either case, it is clear that AGN are prevalent in massive galaxies currently falling off the MS.

ACKNOWLEDGEMENTS

The authors thank A. Saintonge for providing the merger classifications for COLD GASS as well as for thoughtful discussion. They are grateful to S. Veilleux for helpful discussions and a careful reading. They also thank the anonymous referee for a detailed review that greatly improved the quality of this paper. This research has made use of the NASA/IPAC Extragalactic Database (NED) which is operated by the Jet Propulsion Laboratory, California Institute of Technology, under contract with the National Aeronautics and Space Administration. This publication makes use of data products from the *Wide-field Infrared Survey Explorer*, which is a joint project of the University of California, Los Angeles, and the Jet Propulsion Laboratory/California Institute of Technology, funded by the National Aeronautics and Space Administration. Funding for SDSS-III has been provided by the Alfred P. Sloan Foundation, the Participating Institutions, the National Science Foundation, and the US Department of Energy Office of Science. The SDSS-III website is http://www.sdss3.org/. All figures in this publication were made using the MATPLOTLIB PYTHON package (Hunter 2007). This research made use of ASTROPY, a community-developed core PYTHON package for Astronomy (Astropy Collaboration 2013, http://www.astropy.org).

REFERENCES

Antonucci R., 1993, ARA&A, 31, 473
Astropy Collaboration, 2013, A&A, 558, A33
Auld R. et al., 2013, MNRAS, 428, 1880
Baldwin J. A., Phillips M. M., Terlevich R., 1981, PASP, 93, 5
Barthelmy S. D. et al., 2005, Space Sci. Rev., 120, 143
Baum S. A. et al., 2010, ApJ, 710, 289
Baumgartner W. H., Tueller J., Markwardt C. B., Skinner G. K., Barthelmy S., Mushotzky R. F., Evans P. A., Gehrels N., 2013, ApJS, 207, 19
Best P. N., 2007, New Astron. Rev., 51, 168
Bianchi L., Conti A., Shiao B., 2014, Adv. Space Res., 53, 900
Boselli A., Boissier S., Cortese L., Gil de Paz A., Seibert M., Madore B. F., Buat V., Martin D. C., 2006, ApJ, 651, 811
Boselli A. et al., 2010, PASP, 122, 261
Boselli A. et al., 2012, A&A, 540, A54
Boselli A., Hughes T. M., Cortese L., Gavazzi G., Buat V., 2013, A&A, 550, A114
Bouwens R. J. et al., 2012, ApJ, 754, 83
Brinchmann J., Charlot S., White S. D. M., Tremonti C., Kauffmann G., Heckman T., Brinkmann J., 2004, MNRAS, 351, 1151
Bruzual G., Charlot S., 2003, MNRAS, 344, 1000
Buchanan C. L., Gallimore J. F., O'Dea C. P., Baum S. A., Axon D. J., Robinson A., Elitzur M., Elvis M., 2006, AJ, 132, 401
Calzetti D. et al., 2010, ApJ, 714, 1256
Cardamone C. N., Urry C. M., Schawinski K., Treister E., Brammer G., Gawiser E., 2010, ApJ, 721, L38
Casey C. M., 2012, MNRAS, 425, 3094
Catinella B. et al., 2010, MNRAS, 403, 683
Charlot S., Longhetti M., 2001, MNRAS, 323, 887
Chary R., Elbaz D., 2001, ApJ, 556, 562
Chen C.-T. J. et al., 2013, ApJ, 773, 3
Cicone C. et al., 2014, A&A, 562, A21
Ciesla L. et al., 2012, A&A, 543, A161
Ciesla L. et al., 2014, A&A, 565, A128
Cimatti A. et al., 2013, ApJ, 779, L13
Cortese L. et al., 2010, A&A, 518, L49
Cortese L. et al., 2012a, A&A, 540, A52
Cortese L. et al., 2012b, A&A, 544, A101
Cortese L. et al., 2014, MNRAS, 440, 942
Croton D. J. et al., 2006, MNRAS, 365, 11
Dale D. A., Helou G., 2002, ApJ, 576, 159 (DH02)
Dale D. A. et al., 2007, ApJ, 655, 863
Domínguez Sánchez H. et al., 2014, MNRAS, 441, 2
Draine B. T., 2003, ARA&A, 41, 241
Dubois Y., Gavazzi R., Peirani S., Silk J., 2013, MNRAS, 433, 3297
Elbaz D. et al., 2007, A&A, 468, 33
Elbaz D. et al., 2011, A&A, 533, A119
Fabian A. C., 2012, ARA&A, 50, 455
Feigelson E. D., Nelson P. I., 1985, ApJ, 293, 192
Ferrarese L., Merritt D., 2000, ApJ, 539, L9
Galametz M. et al., 2012, MNRAS, 425, 763
Gebhardt K. et al., 2000, ApJ, 539, L13
Gehrels N. et al., 2004, ApJ, 611, 1005
Gordon K. D. et al., 2010, A&A, 518, L89
Griffin M. J. et al., 2010, A&A, 518, L3
Gültekin K. et al., 2009, ApJ, 698, 198
Häring N., Rix H.-W., 2004, ApJ, 604, L89
Harrison C. M., Alexander D. M., Mullaney J. R., Swinbank A. M., 2014, MNRAS, 441, 3306
Heckman T. M., Blitz L., Wilson A. S., Armus L., Miley G. K., 1989, ApJ, 342, 735
Heinis S. et al., 2014, MNRAS, 437, 1268
Hickox R. C. et al., 2009, ApJ, 696, 891
Hickox R. C., Mullaney J. R., Alexander D. M., Chen C.-T. J., Civano F. M., Goulding A. D., Hainline K. N., 2014, ApJ, 782, 9
Hönig S. F., Kishimoto M., 2010, A&A, 523, A27
Hopkins P. F., Quataert E., 2010, MNRAS, 407, 1529
Hunter J. D., 2007, Comput. Sci. Eng., 9, 90
Isobe T., Feigelson E. D., Akritas M. G., Babu G. J., 1990, ApJ, 364, 104
Kauffmann G. et al., 2003, MNRAS, 346, 1055
Kaviraj S., Schawinski K., Silk J., Shabala S. S., 2011, MNRAS, 415, 3798
Keel W. C. et al., 2012, MNRAS, 420, 878
Keel W. C. et al., 2015, AJ, 149, 155
Kennicutt R. C., Jr, 1998, ARA&A, 36, 189
Kennicutt R. C., Evans N. J., 2012, ARA&A, 50, 531
Kocevski D. D. et al., 2012, ApJ, 744, 148
Kormendy J., Richstone D., 1995, ARA&A, 33, 581
Koss M., Mushotzky R., Veilleux S., Winter L., 2010, ApJ, 716, L125
Koss M., Mushotzky R., Veilleux S., Winter L. M., Baumgartner W., Tueller J., Gehrels N., Valencic L., 2011, ApJ, 739, 57
Kovács A. et al., 2010, ApJ, 717, 29
Lilly S. J., Carollo C. M., Pipino A., Renzini A., Peng Y., 2013, ApJ, 772, 119
Lintott C. J. et al., 2008, MNRAS, 389, 1179
Lintott C. J. et al., 2009, MNRAS, 399, 129
Magnelli B. et al., 2014, A&A, 561, A86
Magorrian J. et al., 1998, AJ, 115, 2285
Maiolino R., Ruiz M., Rieke G. H., Keller L. D., 1995, ApJ, 446, 561
Marconi A., Hunt L. K., 2003, ApJ, 589, L21
Martin D. C. et al., 2005, ApJ, 619, L1
Martin D. C. et al., 2007, ApJS, 173, 342
Meléndez M., Mushotzky R. F., Shimizu T. T., Barger A. J., Cowie L. L., 2014, ApJ, 794, 152
Mullaney J. R., Alexander D. M., Goulding A. D., Hickox R. C., 2011, MNRAS, 414, 1082
Mullaney J. R. et al., 2012a, MNRAS, 419, 95
Mullaney J. R. et al., 2012b, ApJ, 753, L30
Murphy E. J. et al., 2011, ApJ, 737, 67
Mushotzky R. F., Shimizu T. T., Meléndez M., Koss M., 2014, ApJ, 781, L34

Nandra K. et al., 2007, ApJ, 660, L11
Nenkova M., Sirocky M. M., Ivezić Ž., Elitzur M., 2008, ApJ, 685, 147
Netzer H. et al., 2007, ApJ, 666, 806
Neugebauer G. et al., 1984, ApJ, 278, L1
Noeske K. G. et al., 2007, ApJ, 660, L43
Novak G. S., Ostriker J. P., Ciotti L., 2011, ApJ, 737, 26
Ott S., 2010, in Mizumoto Y., Morita K.-I., Ohishi M., eds, ASP Conf. Ser. Vol. 434, Astronomical Data Analysis Software and Systems XIX. Astron. Soc. Pac., San Francisco, p. 139
Patton D. R., Atfield J. E., 2008, ApJ, 685, 235
Peebles P. J. E., 1972, ApJ, 178, 371
Peng C. Y., Ho L. C., Impey C. D., Rix H.-W., 2002, AJ, 124, 266
Peng Y.-j. et al., 2010, ApJ, 721, 193
Pierce C. M. et al., 2010, MNRAS, 408, 139
Pilbratt G. L. et al., 2010, A&A, 518, L1
Poglitsch A. et al., 2010, A&A, 518, L2
Rodighiero G. et al., 2010, A&A, 518, L25
Rosario D. J. et al., 2012, A&A, 545, A45
Rosario D. J. et al., 2013a, ApJ, 763, 59
Rosario D. J. et al., 2013b, ApJ, 771, 63
Roussel H., 2013, PASP, 125, 1126
Saintonge A. et al., 2011a, MNRAS, 415, 32
Saintonge A. et al., 2011b, MNRAS, 415, 61
Saintonge A. et al., 2012, ApJ, 758, 73
Salim S. et al., 2007, ApJS, 173, 267
Sánchez S. F. et al., 2012, A&A, 538, A8
Sanders D. B., Soifer B. T., Elias J. H., Madore B. F., Matthews K., Neugebauer G., Scoville N. Z., 1988, ApJ, 325, 74
Schawinski K., Virani S., Simmons B., Urry C. M., Treister E., Kaviraj S., Kushkuley B., 2009, ApJ, 692, L19
Schawinski K. et al., 2014, MNRAS, 440, 889
Schweitzer M. et al., 2006, ApJ, 649, 79
Scott D. W., 1992, Multivariate Density Estimation. Wiley, New York
Shao L. et al., 2010, A&A, 518, L26
Silk J., Rees M. J., 1998, A&A, 331, L1
Silverman J. D. et al., 2008, ApJ, 675, 1025
Silverman J. D. et al., 2009, ApJ, 696, 396
Simard L., Mendel J. T., Patton D. R., Ellison S. L., McConnachie A. W., 2011, ApJS, 196, 11
Smith M. W. L. et al., 2012, ApJ, 756, 40
Speagle J. S., Steinhardt C. L., Capak P. L., Silverman J. D., 2014, ApJS, 214, 15
Strateva I. et al., 2001, AJ, 122, 1861
Tombesi F., Meléndez M., Veilleux S., Reeves J. N., González-Alfonso E., Reynolds C. S., 2015, Nature, 519, 436
Trump J. R. et al., 2015, preprint (arXiv:1501.02801)
Tueller J. et al., 2010, ApJS, 186, 378
Ueda Y., Akiyama M., Hasinger G., Miyaji T., Watson M. G., 2014, ApJ, 786, 104
Urry C. M., Padovani P., 1995, PASP, 107, 803
Veilleux S. et al., 2013, ApJ, 776, 27
Viero M. P. et al., 2014, ApJS, 210, 22
Villforth C. et al., 2014, MNRAS, 439, 3342
Vito F. et al., 2014, MNRAS, 441, 1059
Whitaker K. E., van Dokkum P. G., Brammer G., Franx M., 2012, ApJ, 754, L29
Winter L. M., Veilleux S., McKernan B., Kallman T. R., 2012, ApJ, 745, 107
Wright E. L. et al., 2010, AJ, 140, 1868
Wu Y., Charmandaris V., Huang J., Spinoglio L., Tommasin S., 2009, ApJ, 701, 658
Wuyts S. et al., 2011, ApJ, 742, 96
Zibetti S., Charlot S., Rix H.-W., 2009, MNRAS, 400, 1181

APPENDIX A: EXAMPLE FITS TO THE SED OF THE BAT AGN AND HRS

In this appendix, we provide to the reader example SED fits to both the BAT AGN and HRS as well as a brief description of the model and fitting procedure. We chose to fit our SEDs with the model described in Casey (2012), which is a combination of an exponentially cutoff MIR power law and a single-temperature greybody. The greybody has the standard form, $F_\nu \propto \nu^\beta B_\nu(T)$, where β is the dust emissivity spectral index and $B_\nu(T)$ is the standard Planck function with temperature T, and has been shown to fit very well the FIR SEDs of both normal SF galaxies as a whole (Gordon et al. 2010; Galametz et al. 2012; Auld et al. 2013; Cortese et al. 2014) and small SF regions within the galaxy (Galametz et al. 2012; Smith et al. 2012).

The MIR power law, with the form $F_\lambda \propto \lambda^\alpha e^{-(\lambda/\lambda_{\rm turn})^2}$, can be thought of as the sum of many hot dust components that combine to form an overall power law in the broad-band SED (Kovács et al. 2010). Casey (2012) found that this simple model fits the observed SEDs of ULIRGs very well compared to single greybodies and standard SED template libraries (e.g. Chary & Elbaz 2001). While the physical heating mechanism is different between Seyfert galaxies and ULIRGS, the same power-law shape is observed in MIR spectra of AGN (Schweitzer et al. 2006; Mullaney et al. 2011) and motivates the addition of this component for the BAT AGN. The equation for the total model is then

$$F_\nu = N_{\rm pwlw}\nu^{-\alpha}e^{-(\lambda/\lambda_{\rm turn})^2} + N_{\rm grey}\nu^\beta B_\nu(T). \quad \text{(A1)}$$

For each source, we used all wavebands that had at least a 5σ detection. The best-fitting parameters were found from χ^2-minimization using the Levenberg–Marquardt algorithm for optimization. Fig. A1 displays four randomly chosen BAT AGN SEDs and their 1σ uncertainties (black dots with error bars) along with the best-fitting model (black line). The dashed lines indicate the best-fitting MIR cutoff power law (blue) and greybody (red). As shown, the model does quite well for the wide variety of SED shapes in the BAT AGN sample.

Fig. A2 is the same as Fig. A1 except for four randomly chosen HRS sources to show that the model works equally well for the sources without an AGN.

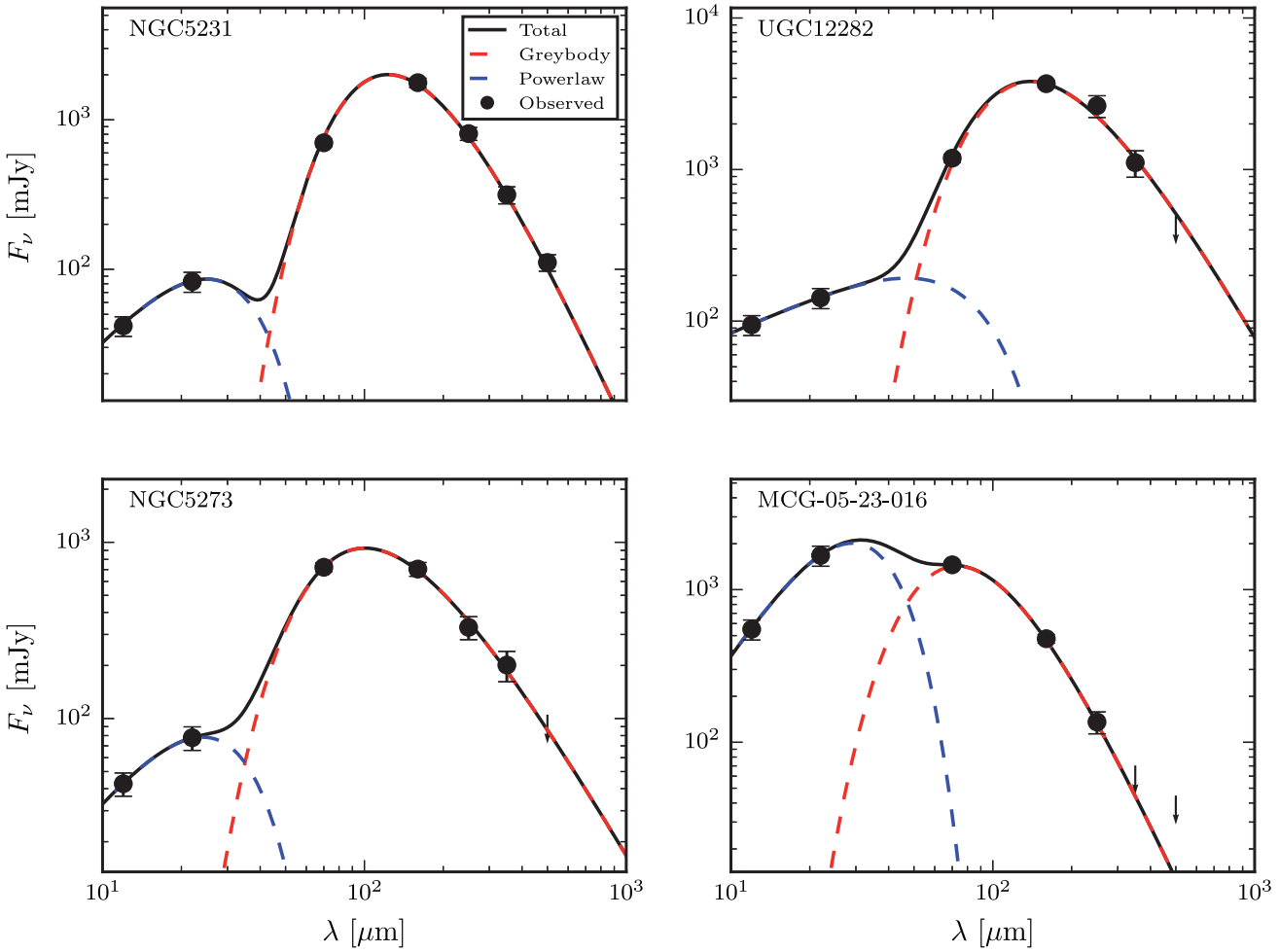

Figure A1. Example SED fits for four randomly chosen BAT AGN used for analysis in this paper. The observed fluxes are shown as black dots with 1σ error bars. 5σ upper limits to the flux for undetected wavebands are shown as downward-pointing arrows. The solid black line is the best-fitting model given by equation (A1) while the dashed blue and red lines indicate the best-fitting MIR power-law and greybody components, respectively. A colour version of this figure is available online.

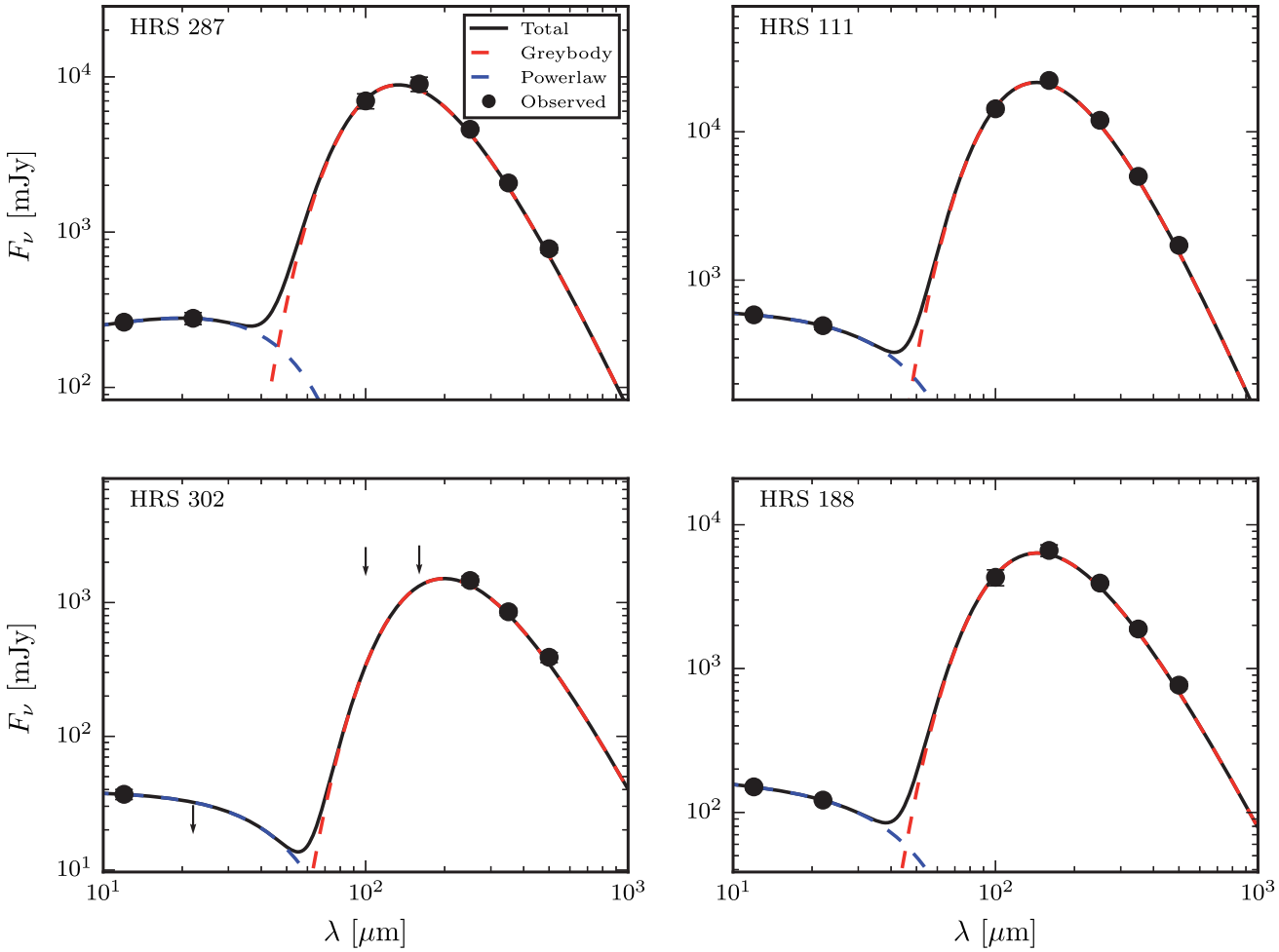

Figure A2. Same as Fig. A1 except for four randomly chosen HRS sources. A colour version of this figure is available online.

This paper has been typeset from a TEX/LATEX file prepared by the author.